

The Influence of Lateral and Top Boundary Conditions on Regional Air Quality Prediction: a Multi-Scale Study Coupling Regional and Global Chemical Transport Models

Youhua Tang¹ (ytang@cgrer.uiowa.edu), Gregory R. Carmichael¹ (gcarmich@engineering.uiowa.edu), Narisara Thongboonchoo¹ (nthongbo@cgrer.uiowa.edu), Tianfeng Chai¹ (tchai@cgrer.uiowa.edu), Larry W. Horowitz² (larry.horowitz@noaa.gov), Robert B. Pierce³ (r.b.pierce@larc.nasa.gov), Jassim A. Al-Saadi³ (j.a.al-saadi@nasa.gov), Gabriele Pfister⁴ (pfister@ucar.edu), Jeffrey M. Vukovich⁵ (jeff_vukovich@unc.edu), Melody A. Avery³ (m.a.avery@larc.nasa.gov), Glen W. Sachse³ (g.w.sachse@larc.nasa.gov), Thomas B. Ryerson⁶ (thomas.b.ryerson@noaa.gov), John S. Holloway⁶ (John.S.Holloway@noaa.gov), Elliot L. Atlas⁷ (eatlas@rsmas.miami.edu), Frank M. Flocke⁴ (ffl@ucar.edu), Rodney J. Weber⁸ (rweber@eas.gatech.edu), L. Gregory Huey⁸ (greg.huey@eas.gatech.edu), Jack E. Dibb⁹ (jack.dibb@unh.edu), David G. Streets¹⁰ (dstreets@anl.gov), and William H. Brune¹¹ (brune@ems.psu.edu)

1. Center for Global and Regional Environmental Research, University of Iowa, Iowa City, Iowa, USA

2. NOAA GFDL Laboratory, Princeton, New Jersey, USA

3. NASA Langley Research Center, Virginia, USA

4. National Center for Atmospheric Research, Boulder, Colorado, USA

5. Carolina Environmental Program (CEP), University of North Carolina at Chapel Hill

6. NOAA Aeronomy Laboratory, Boulder, Colorado, USA

7. University of Miami, Miami, Florida, USA

8. Georgia Institute of Technology, Atlanta, Georgia, USA

9. University of New Hampshire, Durham, NH, USA

10. Argonne National Laboratory, Argonne, Illinois, USA

11. Pennsylvania State University, University Park, PA, USA

Abstract:

The sensitivity of regional air quality model to various lateral and top boundary conditions is studied in 2 scales: 60km domain covering the whole USA and the 12km domain over Northeastern USA. Three global models (MOZART-NCAR, MOZART-GFDL and RAQMS) are used to drive the STEM-2K3 regional model with time-varied lateral and top boundary conditions (BCs). The regional simulations with different global BCs are examined using ICARTT aircraft measurements performed in the summer of 2004, and the simulations are shown to be sensitive to the boundary conditions from the global models, especially for relatively long-lived species, like CO and O₃. For example,

1 differences in the mean CO concentrations from 3 different global-model boundary
2 conditions are as large as 50 ppbv. Over certain model grids, the model's sensitivity to
3 BCs is found to depend not only on the distance from the domain's top and lateral
4 boundaries, downwind/upwind situation, but also on regional emissions and species
5 properties. The near-surface prediction over polluted area is usually not as sensitive to the
6 variation of BCs, but to the magnitude of their background concentrations. We also test
7 the sensitivity of model to temporal and spatial variations of the BCs by comparing the
8 simulations with time-varied BCs to the corresponding simulations with time-mean and
9 profile BCs. Removing the time variation of BCs leads to a significant bias on the
10 variation prediction and sometime causes the bias in predicted mean values. The effect of
11 model resolution on the BC sensitivity is also studied.

12

13 **1. Introduction**

14

15 Lateral and top boundary conditions (BCs) are a major uncertain factor in regional air
16 quality prediction. Mesoscale meteorological models, like MM5, RAMS and WRF,
17 usually use lateral boundary conditions supplied by global meteorological model. In
18 principle, regional chemical transport/air quality model should also import boundary
19 conditions from corresponding global models to consider the external forcing. However,
20 additional uncertainties are introduced in this importing process due to the uncertainties
21 in the global models and differences in resolution etc. In the past, most regional chemical
22 transport models have used fixed concentration profiles as their boundary conditions.
23 These concentration profiles should represent the mean concentrations during the period
24 of interest. Some profiles are based on historical measurements (Winner et al., 1995), and
25 some profiles are set to typical clean concentrations (Chen et al., 2003). Typically the
26 profile boundary conditions lack temporal and spatial variations, and thus the
27 corresponding specific variability in the regional simulation mainly reflects the
28 contribution of emission, transport and chemical processes within the model domain.

29

1 The ICARTT (International Consortium for Atmospheric Research on Transport and
2 Transformation) field experiment was performed in the summer of 2004
3 (<http://www.al.noaa.gov/ICARTT/>), and included NASA INTEX-A (Intercontinental
4 Chemical Transport Experiment -A), the NOAA NEAQS/ITCT-2k4 (New England Air
5 Quality Study - Intercontinental Transport and Chemical Transformation, 2004), and
6 other coordinated studies. During the ICARTT period, the NASA DC-8 aircraft
7 performed 18 research flights covering the continental USA, and the NOAA WP-3
8 aircraft had 18 research flights, mainly over northeastern USA (Figure 1). Some of these
9 flights encountered remote signatures, such as Asian air masses, long-range transported
10 biomass burning plumes, and stratospheric air mass intrusions. Tropospheric regional
11 chemical transport model can not predict these phenomena without appropriate lateral
12 and top boundary conditions. The ICARTT airborne measurements provide an
13 opportunity to examine the performance of a regional model driven by different boundary
14 conditions from different global models. We can also test the dependence of regional
15 model on BCs under different scales.

16

17 In this study we evaluate the sensitivity and performance of regional model predictions to
18 various BC treatments. We specifically employed the regional chemical transport model
19 STEM-2K3 (Tang et al., 2004) with lateral and top boundary conditions from three
20 global models: MOZART-NCAR, MOZART-GFDL and RAQMS. Figure 2 shows the
21 framework of this study. First, we will compare regional model predictions driven by the
22 BCs from three different global models, and evaluate the variations in regional
23 predictions caused by BCs. Next, we will perform study for the model sensitivity to the
24 temporal and spatial variations of BCs by comparing the model prediction with original
25 time-varied BCs to simulations with temporal and spatial averaged BCs. The sensitivity
26 study will be performed in two domains: 60km primary domain covering continental
27 USA and 12km nested domain over Northeastern USA. The detail of these models and
28 methodologies will be described later.

29

30 **2. Methodology Description**

31

1 In this study, we employ the STEM-2K3 (Tang et al., 2004) regional chemical transport
2 model, which is a flexible regional-scale chemical transport model. In this study,
3 SAPRC99 chemical mechanism (Cater, 2000) with on-line photolysis solver (Tang et al,
4 2003a) and SCAPE II (Simulating Composition of Atmospheric Particles at Equilibrium)
5 (Kim et al, 1993a, b; Kim and Seinfeld, 1995) aerosol module were used. MM5
6 meteorological model driven by NCEP FNL (Final Global Data Assimilation System)
7 $1^{\circ} \times 1^{\circ}$ analyzed data every 6 hours was used for the meteorological fields. The STEM
8 model used the same grid system as MM5. The MM5 simulation was performed in a
9 60km domain covering North American (Figure 3), and a one-way nested 12km domain
10 that covered Northeastern USA, with sigma layers extending from surface to 100hPa:
11 0.999, 0.9965, 0.9925, 0.985, 0.97, 0.945, 0.91, 0.87, 0.825, 0.77, 0.71, 0.65, 0.59, 0.53,
12 0.47, 0.41, 0.35, 0.285, 0.21, 0.125, and 0.04. Grid nudging was performed every 6 hours,
13 and re-initialization with FNL data took place every 72 hours. The cloud scheme of Grell
14 et al. (1994) was chosen for the physical parameterization, and MRF scheme (Hong and
15 Pan, 1996) was employed for PBL parameterization.

16

17 **2.1 Emissions**

18

19 During the ICARTT field experiment the U.S. EPA National Emission Inventory (NEI)
20 with base year 1999 was used for forecasting. In this study, the NEI-2001 version 3
21 emission was employed. It should be noted that NEI-2001 and NEI-1999 emissions
22 differ significantly in CO, NO_x and SO₂, and the difference between the forecast and post
23 simulation reflect these emission differences. To reflect systematic differences between
24 the observations and predictions, we adjusted the NEI-2001v3 VOC emissions; light
25 alkanes (ethane and propane) were doubled, and aromatic emissions were reduced by
26 30%. In this study, we also included aviation emissions from the EDGAR emission
27 inventory (Olivier et al., 2001).

28

29 Lightning NO_x emissions were explicitly treated in this study using data from National
30 Lightning Detection Network (NLDN). NLDN data includes hourly lightning location,
31 signal strength and multiplicity in strokes/flash. We used the method of Price et al. (1997)

1 to derive the lightning NO_x emissions, and we used MM5's meteorological information
2 (cloud water content and temperature) to identify the existence of cloud, cloud top and
3 cloud freezing level (Pickering et al., 1998). Both cloud-to-ground (CG) and intra-cloud
4 (IC) flashes were treated and contributed to the NO_x source. The IC/CG ratio is an
5 important factor. Here we adopted the methods of Pickering et al. (1998) and Price et al.
6 (1997) to calculating the lightning NO_x emissions. In the vertical direction, CG lightning
7 NO_x was uniformly distributed from cloud top to ground. The breakthrough potential of
8 the intra-cloud lightning was set at 1/10 of the CG lightning (Price et al., 1997). We set
9 the negative CG lightning NO_x producing rate to 1×10^{17} molecules/J and the positive CG
10 to a value of 1.6 times of this value (Price et al., 1997).

11
12 The biogenic emission inventory system 2 (BEIS 2) (Geron, et al., 1994) was used to
13 generate time-varied isoprene and monoterpene emissions driven by the MM5
14 meteorological fields. During the ICARTT period, forest fires occurred in Alaska and
15 Northwestern Canada, which was out of the regional model domain. However, the lateral
16 boundary conditions from global models provided the time-varied biomass burning CO
17 and other species.

18
19 Sea salt emissions were estimated using the Gong et al (2003) method driven by MM5's
20 10m wind speed. In this study, size-resolved sea salt emissions enter 4 aerosol size bins
21 (in diameter): 0.1 μ m-0.3 μ m, 0.3 μ m-1.0 μ m, 1.0 μ m-2.5 μ m, and 2.5 μ m-10 μ m (Tang et al.,
22 2004).

23

24 **2.2 Top and Lateral Boundary Conditions**

25

26 In this study, lateral and top boundary conditions came from three global models: the
27 MOZART-NCAR (National Center for Atmospheric Research), the MOZART-GFDL
28 (NOAA GFDL laboratory) and the RAQMS (NASA Langley Research Center). The
29 model differences on regional BCs reflect differences in emissions, meteorology,
30 chemical mechanism and treatments of stratospheric ozone and exchanges. These two
31 MOZART (Model for OZone And Related chemical Tracers) (Horowitz et al., 2003)

1 simulations use different configurations: MOZART-NCAR was run by Gabriele Pfister
2 with 2.8 degree horizontal resolution and MOPITT satellite derived forest fire emissions
3 (Pfister et al., 2005), biofuel and fossil fuel emissions of Granier et al., 2004, and NCEP
4 reanalysis meteorology, while MOZART-GFDL was run by Larry Horowitz with 1.89
5 degree horizontal resolution, NCEP reanalysis meteorology, stratospheric O₃ relaxed to
6 climatology, EDGAR Version 2 (1990) (Olivier and Berdowski, 2001) fossil fuel
7 emissions and forest fire emission estimated by Harvard University (Turquety et al.,
8 2005). RAQMS (Real-time Air Quality Modeling System) is multi-scale chemical
9 transport model that can run either globally or regionally (Pierce et al., 2003). During the
10 ICARTT period, RAQMS was run globally at 1.4 degree horizontal resolution with
11 meteorological fields initialized from the NOAA GFS analysis every 6 hours, and
12 included stratospheric ozone profile assimilation in addition to the TOMS column
13 assimilation (Pierce et al., 2006). RAQMS uses climatological emissions for NO_x and CO
14 from GEIA/EDGAR inventory with updated Asian emissions from Streets et al. (2003),
15 biogenic CO from Duncan and Bey (2004) and aircraft NO_x emission from HSRP
16 database (Stolarski et al., 1995). Each global model was used in the analysis of the
17 ICARTT observations, and the further details about the individual models and their
18 differences can be found in Pfister et al. (2005), Horowitz et al., (2003) and Pierce et al.
19 (2006).

20

21 In this study, we imported time-dependent top and lateral boundary conditions for
22 STEM-2K3 from the three global models. Figure 3 shows the mean O₃ top boundary
23 conditions from the three global models used by STEM. STEM's top is the same as the
24 top of MM5, or 100 hPa in MM5's reference atmosphere. Figure 3 also shows the STEM
25 primary domain: 97×62 grids in 60km horizontal resolution. As shown in Figure 3,
26 RAQMS provides the highest O₃ top boundary, and MOZART-GFDL ranks the second,
27 which is similar to RAQMS. The MOZART-NCAR's top boundary is significantly lower
28 than the other two models by up to 100-200 ppbv, especially north of 40°N. MOZART-
29 NCAR uses a synthetic ozone ("SYNOZ") representation (McLinden et al., 2000) in
30 order to constrain the stratospheric flux of ozone (Emmons et al., in preparation).

31

1 Figure 4 shows the corresponding CO lateral boundary conditions from the 3 global
2 models. RAQMS tends to yield 20-40 ppbv lower CO concentrations than the two
3 MOZART models in the south and east boundaries of the STEM 60km domain. Among
4 these three lateral boundary conditions, MOZART-GFDL has the highest mean CO
5 concentrations, and especially it has a higher CO west boundary condition, the major
6 inflow boundary, than the other global models. All of these models have relatively high
7 CO concentrations in the north boundary condition, which mainly come from the forest
8 fire emissions in Alaska and Canada. MOZART-GFDL has the highest biomass burning
9 CO concentration among these 3 models, and these high CO concentration extend from
10 the surface to about 6km. RAQMS's mean CO concentration in the north boundary is
11 similar to MOZART-GFDL, but has a relatively narrow high-CO plume. MOZART-
12 NCAR shows an isolated CO hot spot at the altitude of 7km. These differences reflect
13 their different emission inventories, and different releasing heights of biomass burning
14 sources.

15
16 It should also be noted that both Figures 3 and 4 illustrate the period-mean boundary
17 conditions from the three global models. The simulations used time-varied BCs, which
18 can have much greater differences for certain periods.

19

20 **2.3 Analysis Method for the Sensitivity to Boundary Conditions**

21

22 We examine model's sensitivity to the temporal and spatial variations of BCs (Figure 2).
23 Furthermore, by averaging the boundary conditions inputs spatially and temporally, we
24 can remove the temporal and spatial variations in the BCs. Simulations with temporally
25 and spatially averaging BCs are performed to evaluate the effect of averaging BC on the
26 regional prediction, or the sensitivity of the regional prediction to the temporal and spatial
27 variations of BCs. These studies are performed for 60km and 12km domains.

28

29 **3. Comparison of Different Boundary Conditions**

30

1 We performed three STEM regional simulations driven by the three boundary conditions,
2 and compared these simulations with aircraft measurements for the ICARTT period. The
3 three STEM simulations used the same emission and settings except for their top and
4 lateral boundary conditions. At first, we present results for specific ICARTT flights to
5 illustrate the sensitivity of the regional predictions to the BCs in several scenarios.

7 **3.1 DC-8 flight on July 15**

8
9 The 8th DC-8 flight was a transit research flight from St. Louis to New Hampshire. This
10 flight encountered a concentrated plume transported from the northwest boundary at
11 around 16 UTC.

12
13 Figure 5 shows the DC-8 flight path (Figure 5A) along with the O₃ and CO horizontal
14 distributions predicted with the three BCs in 10km at 15UTC. Figure 6 shows the
15 comparison of CO and O₃ between the observation and the simulations with the three
16 boundary conditions. All simulations captured the similar general features that were
17 observed. The STEM simulations with MOZART-GFDL and RAQMS BCs tend to have
18 higher O₃ concentrations for altitudes > 6km, and the simulation with MOZART-NCAR
19 produced the values closest to the observation. Since all the STEM simulations used the
20 same emissions and other settings, these differences come from the differences in the top
21 and lateral boundary conditions. It should be noted that the O₃ overestimations of
22 MOZART-GFDL and RAQMS in this event are not systemic, and later we will see their
23 performances for other scenarios. Figure 6 also shows that the simulated CO with
24 RAQMS BCs is similar to that with MOZART-GFDL BCs, and higher than that with
25 MOZART-NCAR BCs. These differences are consistent with the differences in the
26 corresponding BC concentrations (Figure 3). During the flight segment 15-16 UTC, the
27 DC-8 aircraft encountered an elevated concentrated plume which could be either a long-
28 range transported Asian airmass or a biomass burning plume from Alaska and
29 Northwestern Canada, and the observed CO concentrations increased along with the
30 altitude. Figure 6 shows that none of the simulations completely captured this feature.
31 However, all the CO simulations show slight enhancement around 15:10UTC, implying

1 that they captured part of this feature though the enhancement is not as strong and broad
2 as the measurements due to the coarse resolution of the global models or an
3 underestimation of the forest fire plumes.

4
5 The O₃ and CO predictions show qualitatively similar distributions but with significant
6 differences in absolute concentrations. For examples, during the flight segment 13 –19
7 UTC, the aircraft encountered northwest winds, and the simulation with the MOZART-
8 NCAR top boundary conditions yields much lower O₃ concentrations than those with
9 MOZART-GFDL and RAQMS. In the 10km layer, the simulation with MOZART-
10 NCAR BCs does not have O₃ concentrations over 160 ppbv, but the other two
11 simulations yield O₃ concentrations > 200 ppbv. In the northwestern corner, the RAQMS
12 BCs yields O₃ > 250 ppbv. However, all of the simulations show the high-concentration
13 center around 85°W, 42°N. The simulated CO with MOZART-NCAR BCs is about 20
14 ppbv lower than the other two simulations in the whole field. RAQMS tends to have
15 lower CO contrast than the two MOZART models in STEM’s inflow lateral boundary. In
16 the air stream from the northwest direction (western side of the trough), the simulations
17 with MOZART-NCAR and MOZAR-GFDL BCs have CO enhancements > 20 ppbv
18 compared with their own backgrounds (Figures 5D, 5E), but the corresponding CO
19 enhancement in the simulation with RAQMS BCs is less than 10 ppbv (Figure 5F). In
20 this case, STEM predicted CO concentrations are strongly influenced by the lateral
21 boundary conditions, and its O₃ predictions rely on both top and lateral boundary
22 conditions. Figure 6 show that the three simulations have similar low-altitude O₃
23 concentrations though their high-altitude concentrations differ significantly. On the other
24 hand, the CO concentration differences keep the nearly same pattern in high and low
25 altitudes. It implies that high-altitude O₃ prediction could be more sensitive to top
26 boundary conditions due to the stratospheric influence.

27 28 **3.2 WP-3 flight on July 28**

29
30 Most NOAA WP-3 flights during the ICARTT period departed from Portsmouth, New
31 Hampshire. In July 28, the WP-3 aircraft performed a south-north flight to eastern

1 Canada and back (Figure 7A). During this flight, the aircraft encountered western and
2 southwestern airflows in the middle troposphere. Figure 7 shows the O₃ and CO
3 concentrations in the 5.6km layer by the three simulations driven by the three boundary
4 conditions. All the simulations show similar large-scale features, but with significant
5 differences in the concentration magnitude and gradients. The simulation with RAQMS
6 BCs has the highest O₃ among the three simulations in this layer. In this event, most of
7 the differences come from the northern lateral boundary. In Figure 8, we plotted the
8 observations, and the modeled mean, maximum, and minimum values produced by the
9 ensemble members, which reflects the variability due to different BCs. For the flight
10 segments just after takeoff and before landing, there is little difference in the predictions
11 for O₃, CO and NO_y, reflecting the importance of the regional and local emissions and the
12 relatively weak influence of BCs. The predictions show that a forest fire plume from
13 northwestern Canada appeared at around 16UTC (Figure 8 and Figure 7D), while the
14 observed CO spike appeared at around 16:40UTC. This time shift may be caused by the
15 model resolution, wind prediction and transport process. The predictions for this CO
16 plume differ up to 150 ppbv (maximum - minimum). NO_x tends to be co-emitted with CO
17 from forest fires and is correlated to variety of species comprising NO_y during its
18 transformation (Tang et al, 2003b). Figure 8 shows that observed NO_y has a similar
19 variation to CO from 15 to 17 UTC, and the ensemble prediction captured the NO_y signal
20 of this biomass burning plume but shifted its location and time. In this flight, the O₃ peak
21 concentration appeared at 17:15UTC, which did not overlap with the CO and NO_y peaks,
22 and implied that the O₃ spike could come from other sources, such as stratospheric inflow.
23 The model predictions also showed significant differences on O₃ predictions, which is up
24 to 40 ppbv from 15UTC to 18UTC due to the differences among the global models.

25

26 **4. Influence of Temporal and Spatial Variations of Boundary** 27 **Conditions**

28

29 We have discussed the impact of different boundary conditions imported from different
30 global models. However, this impact just reflects the influence due to different coupled

1 models. In the absence of dynamic BCs from global models, regional air quality models
2 usually use predefined profiles as boundary conditions. Predefined profile BCs are
3 designed to yield reasonable background concentrations for long-lived species, but lack
4 temporal and/or spatial variations. Under some situations for some species, the magnitude
5 of the background concentration is much greater than its spatial and temporal variations,
6 and these variations become less important for certain predictions. This is the reason that
7 predefined profile BCs are useful in regional air quality prediction. Here we perform the
8 sensitivity studies in two scales: 60km and 12km, to test the impact of temporal and
9 spatial averaging of the BCs on regional predictions.

10
11 Figure 2 shows the framework of this study. Here we use the STEM 60km simulation
12 with MOZART-NCAR BCs as the base case. By performing a temporal average of the
13 lateral and top BCs provided by MOZART-NCAR that cover the entire ICARTT period,
14 we get the temporal mean BCs for the 60km domain. Through further horizontal
15 averaging of the time-mean lateral boundary condition along its south, north, east and
16 west boundaries, respectively, we get the profile-equivalent lateral BCs: 4 vertical
17 profiles for each species. With these three BCs (original time-varying, time-mean, and
18 profile), we have 3 corresponding simulations in the 60km domain. The simulation with
19 profile BCs uses the same top BC as that with time-mean BCs. We also performed 3
20 simulations with the one-way nested 12km domain covering the Northeastern United
21 States, using original, time-fixed and profile BCs derived from the 60km simulation with
22 the original MOZART-NCAR BCs (Figure 2). Through comparing these simulations, we
23 can test the model's sensitivity to temporal and spatial variation of BCs at different scales.
24 During the ICARTT period, the NASA DC-8 flights covered nearly the entire continental
25 USA, and the NOAA WP-3 flights mainly flew over Northeastern USA and surrounding
26 area and captured more of the fine structure of urban plumes. In this section, we compare
27 the 60km simulations to the DC-8 airborne measurements, and the 12km simulations to
28 the WP-3 observations.

29
30 Both the NASA DC-8 and NOAA WP-3 aircrafts had flights on July 31. The DC-8
31 aircraft headed to the central North Atlantic and flew back to New Hampshire. Figure 9A

1 shows the 60km CO simulations compared to the aircraft measurement for the returning
2 segment after 21.5 UTC, and the corresponding flight path is shown in Figure 9B. Both
3 the simulations with time-mean and profile BCs tend to overpredict CO by 10-20 ppbv,
4 and the simulation with the original MOZART-NCAR BCs has the best result compared
5 to the measurement. The prediction bias in the profile-BCs simulation is higher than that
6 in time mean BCs. Air masses encountered by this flight mainly come from south and
7 southwest directions (Figure 9). The CO simulation in the 3km layer with original BCs
8 shows that the inflow CO concentration near the southern inflow boundary region
9 affected this flight is around 70-80ppbv. The simulated CO with time-mean BCs is about
10 5-20 ppbv higher than that with the original BCs near the southern inflow boundary, and
11 the corresponding difference between the original and profile BCs is even higher. The
12 biggest CO differences appeared near northern inflow boundary with values to 70 ppbv in
13 the 3km layer.

14
15 On the same day, the NOAA WP-3 aircraft performed a nighttime flight over New
16 England area and sampled the Boston plume. Figure 10 shows the 12km simulated CO
17 and O₃ concentrations compared to aircraft observation for the segment 23-25 UTC. This
18 flight segment is shown in Figure 11, which also shows the nested 12km domain. During
19 this flight, the aircraft changed altitudes between 3km to 500m, but spent most of its time
20 around 1km. The pollutant concentrations could be affected significantly by near-surface
21 or power plant emissions. Figure 10 shows that the simulations with time-fixed and
22 profile BCs tend to overestimate CO and O₃ for this flight segment, while the simulation
23 with original time-varied BCs yields reasonable results. It should be noted that these three
24 simulations show similar variations, and the predicted differences are mainly due to their
25 different background concentrations. The simulation with time-fixed BCs yielded about
26 40 ppbv higher CO and 30 ppbv higher O₃ concentrations than that with original BCs,
27 and the simulation with profile BCs are about 50 and 40 ppbv higher for CO and O₃,
28 respectively. The differences are relatively small at 23 UTC compared with the segment
29 from 24 to 25 UTC. Figure 11 shows that the flight location at 23 UTC is downwind of
30 flight segment at 24-25 UTC. So the difference from the lateral boundary conditions was
31 diluted after the transport. Figure 11 also shows the wind field and simulated

1 concentrations in the model's 1km layer. For this flight segment, the air mass mainly
2 came from south and southwest direction. The 24-25 UTC segment encountered
3 relatively clean air mass from the ocean in the southeast boundary of this domain, and the
4 simulation with original BCs predicted $\text{CO} < 80$ ppbv and $\text{O}_3 < 30$ ppbv near this
5 boundary. For the same area, the simulation with time-fixed BCs showed $\text{CO} > 100$ ppbv
6 and $\text{O}_3 > 50$ ppbv, and the profile-BCs case had $\text{CO} > 130$ ppbv and $\text{O}_3 > 65$ ppbv
7 (Figure 10). This event analysis clearly shows the model's sensitivity to south inflow
8 boundary conditions. During this period, this domain's west boundary was also an inflow
9 boundary. For the area near the domain's west boundary, the simulation with original
10 BCs predicted up to 100 ppbv higher CO and 60 ppbv higher O_3 concentration than the
11 simulations with time-fixed and profile BCs as the temporal averaging reduced the strong
12 inflow signal of this scenario. During this event, the difference between original BCs and
13 profile BCs is greater than that between original BCs and time-fixed BCs, since profile
14 BCs includes less information of variance.

15

16 These results show that the model's sensitivity to the BCs varies from location to location.
17 The locations near the inflow boundaries have the highest sensitivity to the variation of
18 BCs. This event and the flight on July 31 show that clean areas without strong emission,
19 such as ocean, are more sensitive to the BCs than the polluted areas. In another word, the
20 difference of BCs becomes narrowed faster over polluted areas than that over clean areas.

21

22 **5. Overall Evaluation**

23

24 Through the scenario analyses, we showed the regional model's dependence on lateral
25 and top boundary conditions. However, these analyses are based on event cases, and did
26 not give an overall picture. Here we analyze the sensitivity of the model performance to
27 the different BCs using statistical and other methods.

28

29 **5.1 Statistical Results due to Different Global BCs Compared to** 30 **Aircraft Measurements**

1
2 Table 1 shows the correlations between the DC-8 observations and the simulations with
3 boundary conditions from the three global models in three mandatory vertical layers. The
4 statistical results include mean values that represents the concentration magnitudes,
5 correlation coefficient R that reflects the synchronism of the simulations for the temporal
6 and spatial variations, and the correlation slope that reflects the amplitude of the
7 simulated variations compared to observation. The DC-8 flight paths covered nearly the
8 whole USA during the ICARTT period, with altitude ranging from 200m to 12km. Figure
9 1 shows the NASA DC-8 and NOAA WP-3 flight paths during this period. The three
10 simulations have similar performance for O₃ prediction below 3km. The simulation with
11 RAQMS BCs produced the better correlation slope over O₃ above 3km, but its mean O₃
12 concentration is about 9 ppbv higher than the measurements. The 60km simulation with
13 MOZART-GFDL BCs yielded the O₃ mean concentration with the lowest bias below
14 3km. The simulation driven by MOZART-NCAR BCs tended to underestimate O₃, and
15 its variations in the higher altitudes. The simulation with MOZART-GFDL BCs
16 overestimated the mean CO by 10 to 50 ppbv in certain altitudes. The simulation with
17 MOZART-NCAR BCs produced the CO mean concentration with the lowest bias below
18 3km, and the best CO correlation slopes in the three layers. The simulation with RAQMS
19 BCs yields the highest correlation coefficient R in all layers. PAN is an important
20 photochemical species. In this study, our NO_x emission tends to be too higher and yield
21 high mean bias below 3km. The influence of BCs difference on PAN is relatively weak in
22 low altitudes compared to CO or O₃. Above 3km, the simulation with MOZART-NCAR
23 has higher R and better correlation slope, but with higher mean bias.

24
25 A similar comparison for the NOAA WP-3 flights is shown in Table 2. The WP-3 aircraft
26 mainly flew over the northeastern USA with altitudes ranging from 200m to 7km,
27 including many research flights studying urban plumes. Table 2 shows that the 60km
28 simulation with RAQMS BCs has the better overall prediction for O₃ above 3km among
29 these 60km simulations. For the O₃ prediction below 3km, the difference among these
30 simulations is relatively insignificant compared to that for DC-8 flights. The influence of
31 boundary conditions on CO prediction is strong in all layers. The CO prediction with

1 MOZART-NCAR BCs has the lowest mean bias, and the RAQMS has better correlation
2 coefficients in all layers. These three simulations differ little in their predictions of PAN
3 below 3km, implying that regional and local emissions could play a more important role
4 on these emission-related species than the forcing from boundaries over the northeastern
5 USA. In general, the differences among these three simulations for WP-3 flights are
6 smaller than those for DC-8 flights as the DC-8 flew over broader regions and at higher
7 altitudes, and had more flight paths near the domain's lateral and top boundaries. For
8 long-lived high-concentration species, like CO, the influence due to different boundary
9 conditions can be shown throughout the domain. During the ICARTT period, the most
10 significant CO inflow was the forest fire plumes from Alaska and Canada, which entered
11 the STEM 60km domain from its north lateral boundary. The most significant O₃ inflow
12 occurred near the domain top from the stratosphere, which affected DC-8 flights more
13 than WP-3 flights. For most short-lived emitted species, the influence of BCs is relatively
14 weak as the strong emissions within the domain show greater impact.

15
16 Figure 12 shows the CO and O₃ mean vertical profiles and standard deviations for these
17 DC-8 and WP-3 flights. Both aircraft measurements show that the biggest CO standard
18 deviation appears in altitudes from 2.5 to 4km, which reflect the turbulent lofting within
19 the planetary boundary layer (PBL), convection and forest fire plumes. However, none of
20 the simulations captured the magnitude of the observed variation. The simulation with
21 MOZART-GFDL BCs tended to overpredict the mean CO below 6km for the WP-3
22 flights, and below 8km for DC-8 flights, while the simulation driven by MOZART-
23 NCAR BCs underestimated CO above 4km (Figure 12A, 12C). For O₃ prediction, the
24 three simulations have similar behavior below 1km. Above 4km, the simulation with
25 MOZART-NCAR BCs underestimated the O₃ mean concentration, and RAQMS BCs
26 resulted in the O₃ overpredictions above 6km (Figure 12B, 12D). The DC-8 observations
27 show the biggest O₃ mean concentration and standard deviation near the top of
28 troposphere (Figure 12B), where the simulation with MOZART-GFDL BCs best
29 captured the mean O₃ concentration, and MOZART-NCAR tended to underestimate O₃
30 while RAQMS overestimated O₃ in this region. Figure 12B also shows that the
31 MOZART-NCAR model underestimated the O₃ deviation in this top altitude, and the

1 other two global models resulted in larger variations. All observations and models found
2 that the minimum O₃ standard deviation was in the altitude 3-5 km. The small O₃
3 deviation above 6km for WP-3 flights (Figure 12D) is mainly due to its relatively few
4 data points.

5.2 Statistical Results of Model's Sensitivity to Temporal and Spatial Variations of Boundary Conditions

5
6
7
8
9 We also analyzed the difference among the simulations with original time-varied BCs,
10 time-mean BCs and profile BCs in the 60km and 12km domain. Table 3 is similar to
11 Table 1 but for the 60km simulations with original MOZART-NCAR, time-mean and
12 profile boundary conditions. It is evident that the 60km simulation with the original
13 MOZART-NCAR BCs has a better correlation slope and coefficient (R) than those with
14 averaged BCs for O₃, especially in higher altitudes. It is reasonable because temporal and
15 spatial averaging remove O₃ variation information from the top and lateral boundaries. In
16 low altitudes (< 3km), the simulations with averaged BCs have higher mean bias for O₃.
17 However, the time-varied BCs do not show advantage on predicting the mean CO values.
18 Their difference on CO prediction is smaller than that for O₃, because original inflow
19 BCs for the CO do not have variations as strong as for O₃ whose variations are mainly
20 due to stratospheric O₃, except for special events, such as forest fire plumes. Comparison
21 for PAN shows similar results to the O₃ and the time-varied BCs mainly cause difference
22 in high altitudes.

23
24 The corresponding results for 12km simulations compared to NOAA WP-3 observation
25 are shown in Table 4. It should be noted that the 12km domain covered most, but not all
26 of the WP-3 flights. We just chose the flight segments covered by the 12km domain for
27 this comparison. These statistical results do show the advantage of higher resolution as
28 the 12km simulation (Table 4) yielded better correlation coefficients and slopes than the
29 60km simulation (Table 2) for CO, O₃ in low altitudes, as the high resolution could better
30 capture the variations of surface emissions for the WP-3 flight segments over
31 Northeastern USA. The difference among the three BCs is more significant in the 12km

1 simulation than in the 60km simulation. The simulation with original BCs is better than
2 the simulations with time-mean and profile BCs for most species. The advantage of time-
3 varied BCs is shown not only on CO and O₃, but also on PAN. For the 12km domain, the
4 major inflow forcing comes from its upwind areas, including U.S. Midwest and
5 California, with high pollutant emissions. For instance, Chicago is one of major regional
6 contributors to inflow pollutants in the 12km domain. The weather-driven airflow could
7 bring the strong and distinct upwind Chicago signals to this domain. After temporal and
8 spatial averaging, this signal becomes relatively uniform. In the contrast, the 60km
9 domain's inflow boundary is located over relatively clean areas, like the eastern Pacific
10 and Canada, where the natural pollutant signals becomes relatively uniform after long-
11 range transport and dynamical diffusion (except for some special events). So the 60km
12 domain is not as sensitive to the removal of temporal and spatial variations on BCs as the
13 nested 12km domain. In the 12km domain, the time-varied BCs also yield better results
14 for secondary species, such as PAN and O₃.

15
16 To further investigate the model's sensitivity to temporal and spatial variations of
17 boundary conditions and its dependence on location and scale, we compare the predicted
18 CO vertical profiles in the model gridpoints 5 grid cells from the west, east, south and
19 north boundaries of the 60 km simulations in Figure 13, which shows mean values and
20 standard deviations of the predicted/observed concentrations. The west boundary is
21 mainly located along the US west coast, where California emissions are a strong
22 contributor to CO. So, all the three simulations with original, time-mean and profile BCs
23 show similar strong CO deviations at low altitudes, and this deviation decreases with
24 altitude near the west boundary. The biggest difference among these simulations is the
25 CO standard deviation above 9km near the west inflow boundary, where the simulation
26 with original BCs shows much greater variation than the others, though they have similar
27 mean concentration. During the summertime, Asian air mass inflow still exists, but not as
28 strong as that during springtime. The CO standard deviation in the simulation with the
29 original BCs is about 5 ppbv at altitudes above 9km. The other two simulations remove
30 the temporal and both temporal and spatial variations from the lateral boundary, and so
31 their variations become much weaker. The east boundary is the prevailing outflow

1 boundary of this 60km domain, but Figure 13B still shows that the simulation with
2 original BCs yielded greater standard deviations than the simulations with averaged BCs,
3 especially in the high altitudes. Near the south boundary, the simulations have the
4 minimum differences on their standard deviations, even at high altitudes. For the north
5 boundary, these simulations make the biggest difference on the CO standard deviation.
6 The original BCs contain strong and highly time-varied CO inflows, including forest fires
7 and Asian plumes. The simulation with the original MOZART-NCAR BCs shows strong
8 CO variation in the altitudes from 6km to 9km. All simulations with averaged BCs
9 missed this feature, which even produced mean concentration biases (Figure 13D). Figure
10 14 shows the corresponding comparison for the 12km domain covering the northeastern
11 USA. In this domain, the prevailing inflow boundaries are also located in the west and
12 north. The CO variability in the 12km domain is higher than that in the 60km domain,
13 reflecting the difference in regional resolution. The only exception is for the south
14 boundary (Figure 14C), which had weak variations, and all three simulations yielded
15 similar mean CO profiles near the south boundary. Near all the other boundaries, the
16 simulation with original BCs has not only larger CO variations than the two simulations
17 with averaged BCs, but also has a different mean CO profile. Figure 14A shows that the
18 three simulations show similar CO standard deviations below 2km, due to their same
19 emissions, but the mean CO profiles differ significantly, while the simulation with the
20 original BCs yielded the higher CO mean concentration. This simulation also has the
21 higher CO variations in the east and north boundaries at low altitudes. Near all the four
22 boundaries, the simulation with original BCs has higher CO variation in high altitudes
23 than the other two, which is similar to the case in the 60km domain. The CO variation
24 difference among these simulations in low altitudes reflects that the simulations with
25 averaged BCs fail to represent the CO emission and transport from polluted upwind areas,
26 which could immediately adjoin to the model domain.

27

28 **5.3 The Contribution of Lateral Boundary Conditions Represented by** 29 **Influence Functions.**

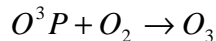
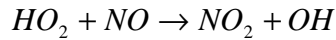
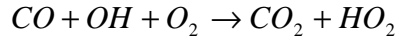
30

1 The above discussion shows that the sensitivity at a given location to boundary
2 conditions depends on the domain characteristics, such as wind field, emissions and
3 strength of boundary flux. To more quantitatively describe these characteristics, we
4 introduce an influence function as

$$5 \quad C_i(x, y, z) = \sum_{n=0}^{N-1} \lambda_i(x, y, z, t) \quad (1)$$

6 where i is the chemical species index, N is the total number of time steps, and $\lambda_i(x, y, z, t)$
7 is the adjoint variable calculated from STEM adjoint model (Sandu et al., 2005; Chai et
8 al., 2006). After choosing a target species and target region at a certain time, $\lambda_i(x, y, z, t)$ is
9 the sensitivity function of the target with respect to $C_i(x, y, z, t)$. Thus, the time-integrated
10 sensitivity, i.e. the influence function $C_i(x, y, z)$, can provide information on how the
11 model predictions are affected by the boundary conditions.. Figure 15 shows the 5-day
12 integrated (July 19-24) $\lambda_{co}(x, y, z)$ (CO as target species) distribution with the MOZART-
13 NCAR boundary condition in our 60km domain for the target subdomain shown in
14 Figure 15A. The target region has a vertical extent from 1 to 4km above ground. From
15 July 19 to 24, the prevailing wind influx to the target region in the 3 km level (Figure
16 15A) came from northwest and southwest, and the southwest wind was relatively weaker.
17 Figure 15A illustrates the vertically integrated influence of the whole-field CO on CO
18 concentrations in the target subdomain. The emission sources from Texas have a strong
19 influence on the target area during this period. In addition to this emission influence, the
20 north boundary condition is the major influencing factor, which extends an area of the
21 influence from northwest boundary to the target area. Figure 15B shows the vertical
22 extent of the CO-on-CO influence function along the cross-section of the north boundary
23 of the 60km domain over continental USA, and we can see that the high influence came
24 from altitudes 1-3 km, and these high CO levels were due to forest fires in Canada and
25 Alaska. Figure 15C shows mean profile of this influence function and its spatial standard
26 deviation along the 4 lateral boundaries during this 5-day period. The north boundary
27 shows the biggest influence on this domain with peak value at ~ 2km, while south
28 boundary's influence existed mainly below 3km. The boundary showed influence above
29 3km due to the CO pollutant from Asia or re-circulated pollutants from U.S west coast.
30 The east boundary has relatively weak influence as it is the prevailing outflow boundary

1 throughout this period. The O₃-on-O₃ influence function is similar to CO-on-CO but its
2 peak values appear at higher altitudes: 3km (Figure 15D), which reflect upper-layer
3 ozone contributions. Figure 15E shows the chemical contribution of CO to O₃ in this
4 influence function. In this case, CO mainly contributes to O₃ photochemical production
5 by pumping NO to NO₂:



7 The west-boundary inflow of CO shows the highest O₃ production efficiency, and the
8 north boundary has the lowest one. This chemical conversion mainly depends on which
9 kinds of air mass mix with the boundary-inflow CO. Near west and south inflow
10 boundaries, there are abundant NO_x emissions that benefit CO contribution to O₃, while
11 the region near the north boundary (north Dakota et al.) are relatively clean.

12

13 **6. Conclusion**

14

15 In this study, we test the influence of boundary conditions from 3 global models on
16 regional chemical transport model, STEM-2K3. Our study shows that STEM's
17 performance is sensitive to BCs for relatively long-lived transported species, such as CO
18 and O₃. The most important advantage of using global model as BCs is that these BCs
19 can bring time-varied external signal to the regional domain, and reflect certain event
20 information, such as biomass burning, stratospheric intrusion, and Asian air mass inflow.
21 Due to the different schemes, configurations, meteorology and emissions, the three global
22 models, MOZART-NCAR, MOZART-GFDL and RAQMS show different performance
23 during the ICARTT period. In generally, RAQMS has the highest O₃ concentration,
24 especially near top of troposphere, where MOZART-NCAR has the lowest O₃ among
25 them. Although they differ so significantly, it is interesting that none of these models has
26 systematical bias compared to aircraft observed O₃ (except in the upper troposphere), and
27 their performances varied from case to case. As shown by the case studies, the simulation
28 with MOZART-NCAR BCs yields better O₃ result in DC-8 flight 8 on July 15, and the

1 simulation with RAQMS BC successfully capture the O₃ peak value in WP-3 flight on
2 July 28. Among these models, MOZART-NCAR has the lowest CO and O₃ predictions,
3 and MOZART-GFDL has the highest mean CO concentration, while RAQMS has the
4 highest O₃ top boundary conditions. In this study, we just focus on O₃ and CO as an
5 example while these models' differences on other species could also be significant.
6 STEM's sensitivity to time-varied BCs is also varied from case to case. In general, the
7 regional model is very sensitive to BCs over the grids near inflow boundaries, such as
8 high altitudes and northern inflow boundary. The model's sensitivity to BCs also depends
9 on the strength of regional and local emissions. If local emission is overwhelmingly
10 strong, such as in urban sites, the model prediction near ground becomes less sensitive to
11 variation of BCs, but to its background magnitude.

12

13 Our study about regional model's sensitivity to the temporal and spatial variation of BCs
14 tells a similar story. Our analysis indicates that even if none of the global boundary
15 conditions is perfect, they can still drive the regional model to yield better results than
16 that with pre-defined profile BCs, especially in correlations with aircraft measurements,
17 since global models can bring time-varied external signals. Boundary conditions are more
18 important to small domain than to big domain. Our sensitivity study shows the model has
19 higher dependence on lateral boundaries in 12km domain than that in 60km domain, as
20 the 12km domain has more distinguished inflow signal due to its locations. In the 12km
21 domain, the BCs in low altitudes could be more important as the high concentrated
22 pollutant inflow exists in lower levels, and even some short-lived species, like SO₂, could
23 be affected. This analysis shows that small-scale high-resolution predictions are more
24 sensitive to boundary conditions and their variations than the large-scale prediction.

25

26 From this study, we can expect to get better prediction by ensemble of the global
27 boundary conditions since each of them has advantage from case to case. During the
28 summertime, continental-scale regional prediction over ground is not very sensitive to
29 lateral boundary conditions since these BCs are not highly varied, but these BCs are still
30 important for the prediction in elevated levels. For finer scale simulation, like urban air
31 quality prediction, the time-varied BCs that includes external inflow is very necessary

1 and predefined BCs can not be reasonably used in this case. It should be noted that this
2 study covers only ICARTT period (about 1.5 months) and focuses on certain events.
3 Further study with longer time range would help better answer this issue.

4

5 **Acknowledgement:**

6 This work was supported in part by grants from the NASA Tropospheric Chemistry
7 Program, the NOAA Global Change Program, and the NSF Atmospheric Chemistry/ITR
8 programs.

1 **Reference:**

- 2
- 3 Carter, W., 2000, Documentation of the SAPRC-99 chemical mechanism for voc
4 reactivity assessment, Final Report to California Air Resources Board Contract
5 No. 92-329, University of California-Riverside, May 8.
- 6 Chai, T. G. R. Carmichael, A. Sandu, Y. Tang and D. N. Daescu, 2006, Chemical data
7 assimilation of transport and chemical evolution over the Pacific (TRACE-P)
8 aircraft measurements, *J. Geophys. Res.*, *111*, D02301, doi:
9 [10.1029/2005JD005883](https://doi.org/10.1029/2005JD005883).
- 10 Chen, K. S., Y. T. Ho, C. H. Lai, Y.-M. Chou, 2003, Photochemical modeling and
11 analysis of meteorological parameters during ozone episodes in Kaohsiung,
12 Taiwan, *Atmos. Environ.*, *37*, 1811-1823.
- 13 Duncan, B. N., I. Bey 2004, A modeling study of the export pathways of pollution from
14 Europe: Seasonal and interannual variations (1987–1997), *J. Geophys. Res.*, *109*,
15 D08301, doi:[10.1029/2003JD004079](https://doi.org/10.1029/2003JD004079).
- 16 Geron, C. D., A. B. Guenther, and T. E. Pierce, 1994, An improved model for estimating
17 emissions of volatile organic-compounds from forests in the eastern united-states.
18 *J. Geophys. Res.*, *99* (D6): 12773-12791.
- 19 Gong, S. L., 2003, A parameterization of sea-salt aerosol source function for sub- and
20 super-micron particles, *Global Biogeochem. Cycles*, *17*(4), 1097,
21 doi:[10.1029/2003GB002079](https://doi.org/10.1029/2003GB002079).
- 22 Granier, C., et al., 2004, Present and future surface emissions of atmospheric compounds,
23 *Rep. EVK 2199900011*, Eur. Comm., Brussels.
- 24 Grell, G. A., J. Dudhia and D. R. Stauffer, 1994, A description of the fifth-generation
25 Penn State/NCAR mesoscale model (MM5). NCAR Technical Note, NCAR/TN-
26 398+STR, 117 pp.
- 27 Hong, S.-Y., and H.-L. Pan, 1996, Nonlocal boundary layer vertical diffusion in a
28 medium-range forecast model. *Mon. Wea. Rev.*, *124*, 2322-2339.
- 29 Kim Y. P., J. H. Seinfeld, and P. Saxena, 1993a, Atmospheric gas-aerosol equilibrium I:
30 Thermodynamic model, *Aerosol Sci. Technol.*, *19*, 151-181.
- 31 Kim Y. P., J. H. Seinfeld, and P. Saxena, 1993b, Atmospheric gas-aerosol equilibrium II:
32 Analysis of common approximations and activity coefficient calculation methods,
33 *Aerosol Sci. Technol.*, *19*, 182-198.
- 34 Kim Y. P., and J. H. Seinfeld, 1995, Atmospheric gas-aerosol equilibrium III:
35 Thermodynamics of crustal elements Ca^{2+} , K^+ , Mg^{2+} , *Aerosol Sci. Technol.*, *22*,
36 93-110.
- 37 McLinden, C.A., S.C. Olsen, B. Hannegan, O. Wild, and M. J. Prather, 2000,
38 Stratospheric ozone in 3-D models: A simple chemistry and the cross-tropopause
39 flux, *J. Geophys. Res.*, *105*(D11), 14,653-14,665.
- 40 Olivier, J. G. J. and J. J. M. Berdowski, 2001, Global emissions sources and sinks. In:
41 Berdowski, J., Guicherit, R. and B.J. Heij (eds.) "The Climate System", pp. 33-78.
42 A.A. Balkema Publishers/Swets & Zeitlinger Publishers, Lisse, The Netherlands.
43 ISBN 90 5809 255 0.
- 44 Pfister, G., P. G. Hess, L. K. Emmons, J.-F. Lamarque, C. Wiedinmyer, D. P. Edwards, G.
45 Pétron, J. C. Gille, and G. W. Sachse, 2005, Quantifying CO emissions from the

1 2004 Alaskan wildfires using MOPITT CO data, *Geophys. Res. Lett.*, 32, L11809,
2 doi:10.1029/2005GL022995.

3 Pickering, K. E., Y. Wang, W.-K. Tao, C. Price, and J.-F. Müller, 1998, Vertical
4 distributions of lightning NO_x for use in regional and global chemical transport
5 models, *J. Geophys. Res.*, 103(D23), 31203-31216.

6 Pierce, R. B., et al., 2003, Regional Air Quality Modeling System (RAQMS) predictions
7 of the tropospheric ozone budget over east Asia, *J. Geophys. Res.*, 108(D21),
8 8825, doi:10.1029/2002JD003176.

9 Pierce, R. B., et al., 2006, Chemical Data Assimilation Estimates of Continental US
10 ozone and Nitrogen budgets during INTEX-A, *Submitted to the Journal of*
11 *Geophysical Research, INTEX Issue.*

12 Price, C. and J. Penner, 1997, NO_x from lightning 1: global distribution based on
13 lightning physics. *J. Geophys. Res.*, 102(D5), 5929-5941.

14 Sandu, A., D. Daescu, G. R. Carmichael and T. Chai, 2005, Adjoint sensitivity analysis
15 of regional air quality models, *J. Comput. Phys.*, 204(1), 222-252.

16 Stolarski, R. S., S. L. Baughcan, W. H. Brune, A. R. Douglass, D. W. Fahey, R. R. Friedl,
17 S. C. Liu, R. A. Plumb, L. R. Bole, H. Wesoky, and D. R. Worsnop, 1995, 1995
18 Scientific Assessment of the Atmospheric Effects of Stratospheric Aircraft, *NASA*
19 *Reference Publication 1381.*

20 Streets, D. G., et al., 2003, An inventory of gaseous and primary aerosol emissions in
21 Asia in the year 2000, *J. Geophys. Res.*, 108 (D21), 8809,
22 doi:10.1029/2002JD003093.

23 Tang, Y., G. R. Carmichael, I. Uno, J.-H. Woo, G. Kurata, B. Lefer, R. E. Shetter, H.
24 Huang, B. E. Anderson, M. A. Avery, A. D. Clarke and D. R. Blake, 2003a,
25 Impacts of aerosols and clouds on photolysis frequencies and photochemistry
26 during TRACE-P, part II: three-dimensional study using a regional chemical
27 transport model, *J. Geophys. Res.*, 10.1029/2002JD003100.

28 Tang, Y., G. R. Carmichael, J.-H. Woo, N. Thongboonchoo, G. Kurata, I. Uno, D. G.
29 Streets, D. R. Blake, R. J. Weber, R. W. Talbot, Y. Kondo and H. B. Singh, 2003b,
30 The Influences of Biomass Burning during TRACE-P Experiment Identified by
31 the Regional Chemical Transport Model, *J. Geophys. Res.*, 108(D21), 8824,
32 doi:10.1029/2002JD003110.

33 Tang, Y., G. R. Carmichael, J. H. Seinfeld, D. Dabdub, Rodney J. Weber, B. Huebert, A.
34 D. Clarke, S. A. Guazzotti, D. A. Sodeman, K. A. Prather, I. Uno, J.-H. Woo, D.
35 G. Streets, P. K. Quinn, J. E. Johnson, C.-H. Song, A. Sandu, R. W. Talbot and J.
36 E. Dibb, 2004, Three-dimensional simulations of inorganic aerosol distributions
37 in East Asia during spring 2001, *J. Geophys. Res.*, 109, D19S23,
38 doi:10.1029/2003JD004201.

39 Trainer, M., D. D. Parrish, M. P. Buhr, R. B. Norton, F. C. Fehsenfeld, K. G. Anlauf, J.
40 W. Bottenheim, Y. Z. Tang, H. A. Wiebe, J. M. Roberts, R. L. Tanner, L.
41 Newman, V. C. Bowersox, J. F. Meagher, K. J. Olszyna, M. O. Rodgers, T.
42 Wang, H. Berresheim, K. L. Demerjian and U. K. Roychowdhury, 1993,
43 Correlation of ozone with NO_y in photochemical aged air. *J. Geophys. Res.*,
44 98(D2), 2917-2925.

- 1 Winner, D. A., G. R. Cass, and R. A. Harley, 1995, Effect of alternative boundary
- 2 conditions on predicted ozone control strategy: a case study in Los Angeles area.
- 3 *Atmos. Environ.*, 29(33), 3451-3464.

Table 1. The statistic result of 60km simulations with the three boundary conditions compared with the observations in NASA DC-8 flights 3-20. The correlation slope and coefficient (R) are presented in model (y) versus observation (x).

Species	Observed Mean	60km Simulated with MOZART-NCAR BCs			60km Simulated with MOZART-GFDL BCs			60km Simulated with RAQMS BCs		
		Simulated Mean	Slope	R	Simulated Mean	Slope	R	Simulated Mean	Slope	R
O₃ (ppbv) (< 1 km)	47.0	52.7	0.84	0.71	52.4	0.91	0.71	53.2	0.88	0.72
O₃ (ppbv) (1-3 km)	54.0	56.3	0.77	0.54	55.9	0.82	0.53	57.5	0.80	0.56
O₃ (ppbv) (> 3 km)	77.7	65.0	0.21	0.51	67.8	0.40	0.54	86.4	0.70	0.51
CO (ppbv) (< 1 km)	136.0	137.2	0.94	0.65	179.6	1.66	0.62	150.1	1.27	0.79
CO (ppbv) (1-3 km)	122.4	131.7	1.14	0.69	172.3	2.16	0.65	142.2	1.43	0.80
CO (ppbv) (> 3 km)	102.2	89.3	0.74	0.38	112.0	1.44	0.43	96.0	0.53	0.41
PAN (ppbv) (< 1 km)	0.35	0.61	1.24	0.64	0.63	1.32	0.64	0.59	1.27	0.64
PAN (ppbv) (1-3 km)	0.25	0.68	2.69	0.59	0.70	2.85	0.58	0.65	2.79	0.58
PAN (ppbv) (> 3 km)	0.31	0.41	0.51	0.30	0.33	0.39	0.20	0.28	0.50	0.21

Table 2. The statistic result of 60km simulations with the three boundary conditions compared with the observations in all NOAA WP-3 research flights. The correlation slope and coefficient (R) are presented in model (y) versus observation (x).

Species	Observed Mean	60km Simulated with MOZART-NCAR BCs			60km Simulated with MOZART-GFDL BCs			60km Simulated with RAQMS BCs		
		Simulated Mean	Slope	R	Simulated Mean	Slope	R	Simulated Mean	Slope	R
O ₃ (ppbv) (< 1 km)	56.2	54.6	0.62	0.62	55.0	0.66	0.63	54.9	0.61	0.62
O ₃ (ppbv) (1-3 km)	60.6	63.8	0.72	0.57	63.8	0.75	0.55	65.1	0.71	0.58
O ₃ (ppbv) (> 3 km)	65.1	60.3	0.44	0.42	58.0	0.42	0.35	66.6	0.49	0.47
CO (ppbv) (< 1 km)	158.3	161.7	1.01	0.45	207.6	1.94	0.40	170.2	1.16	0.57
CO (ppbv) (1-3 km)	140.6	148.5	0.78	0.60	191.5	1.31	0.60	163.4	1.25	0.72
CO (ppbv) (> 3 km)	108.6	104.4	0.42	0.46	135.0	0.92	0.49	114.5	0.86	0.67
PAN (ppbv) (< 1 km)	0.46	0.74	0.70	0.47	0.77	0.74	0.48	0.71	0.67	0.45
PAN (ppbv) (1-3 km)	0.43	0.90	0.81	0.51	0.92	0.81	0.49	0.87	0.77	0.49
PAN (ppbv) (> 3 km)	0.32	0.54	0.30	0.26	0.48	0.14	0.12	0.45	0.24	0.22

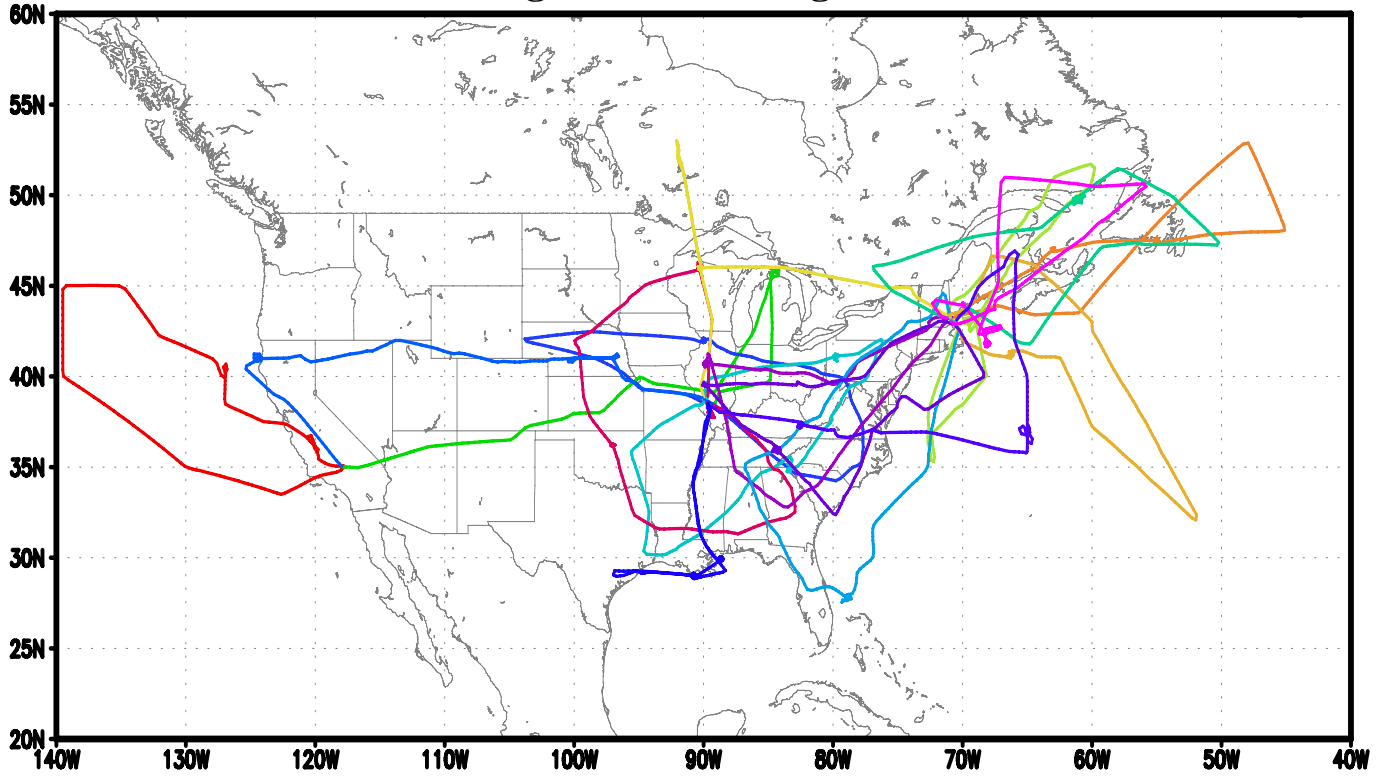
Table 3. The statistic results of 60km simulations with the original MOZART-NCAR, time-mean and profile boundary conditions compared with the observations in NASA DC-8 flights 3-20. The correlation slope and coefficient (R) are presented in model (y) versus observation (x).

Species	Observed Mean	60km Simulated with MOZART-NCAR BCs			60km Simulated with Time-Mean BCs			60km Simulated with Profile BCs		
		Simulated Mean	Slope	R	Simulated Mean	Slope	R	Simulated Mean	Slope	R
O₃ (ppbv) (< 1 km)	47.0	52.7	0.84	0.71	59.2	0.84	0.68	59.3	0.84	0.68
O₃ (ppbv) (1-3 km)	54.0	56.3	0.77	0.54	60.5	0.63	0.54	60.5	0.62	0.54
O₃ (ppbv) (> 3 km)	77.7	65.0	0.21	0.51	65.3	0.18	0.49	64.5	0.17	0.50
CO (ppbv) (< 1 km)	136.0	137.2	0.94	0.65	138.8	0.83	0.65	138.4	0.80	0.64
CO (ppbv) (1-3 km)	122.4	131.7	1.14	0.69	132.8	1.01	0.67	132.0	0.96	0.66
CO (ppbv) (> 3 km)	102.2	89.3	0.74	0.38	90.0	0.58	0.37	89.5	0.49	0.38
PAN (ppbv) (< 1 km)	0.35	0.61	1.24	0.64	0.64	0.78	0.66	0.63	0.78	0.66
PAN (ppbv) (1-3 km)	0.25	0.68	2.69	0.59	0.67	1.14	0.61	0.67	1.13	0.60
PAN (ppbv) (> 3 km)	0.31	0.41	0.51	0.30	0.39	0.16	0.28	0.38	0.17	0.31

Table 4. The statistic result of 12km simulations with the original, time-mean and profile boundary conditions compared with the observations in all NOAA WP-3 research flights covered by the 12km domain. The correlation slope and coefficient (R) are presented in model (y) versus observation (x).

Species	Observed Mean	12km Simulated with Original BCs			12km Simulated with Time-Mean BCs			12km Simulated with Profile BCs		
		Simulated Mean	Slope	R	Simulated Mean	Slope	R	Simulated Mean	Slope	R
O₃ (ppbv) (< 1 km)	56.2	60.1	0.77	0.72	64.7	0.50	0.69	65.5	0.48	0.67
O₃ (ppbv) (1-3 km)	60.6	67.9	0.75	0.59	68.2	0.35	0.42	68.0	0.34	0.42
O₃ (ppbv) (> 3 km)	65.1	62.4	0.36	0.38	55.1	0.07	0.16	54.8	0.10	0.24
CO (ppbv) (< 1 km)	158.3	165.7	1.06	0.54	165.1	0.58	0.47	165.6	0.55	0.44
CO (ppbv) (1-3 km)	140.6	152.9	0.84	0.60	150.5	0.49	0.43	149.7	0.50	0.44
CO (ppbv) (> 3 km)	108.6	104.4	0.42	0.45	102.1	0.13	0.32	101.3	0.15	0.41
PAN (ppbv) (< 1 km)	0.46	0.79	0.72	0.47	0.77	1.26	0.40	0.78	0.43	0.41
PAN (ppbv) (1-3 km)	0.43	0.95	0.63	0.44	0.85	0.37	0.33	0.83	0.41	0.38
PAN (ppbv) (> 3 km)	0.32	0.57	0.40	0.27	0.43	0.12	0.15	0.41	0.19	0.26

NASA DC-8 Flight Paths during ICARTT Period



NOAA WP-3 Flight Paths during ICARTT Period

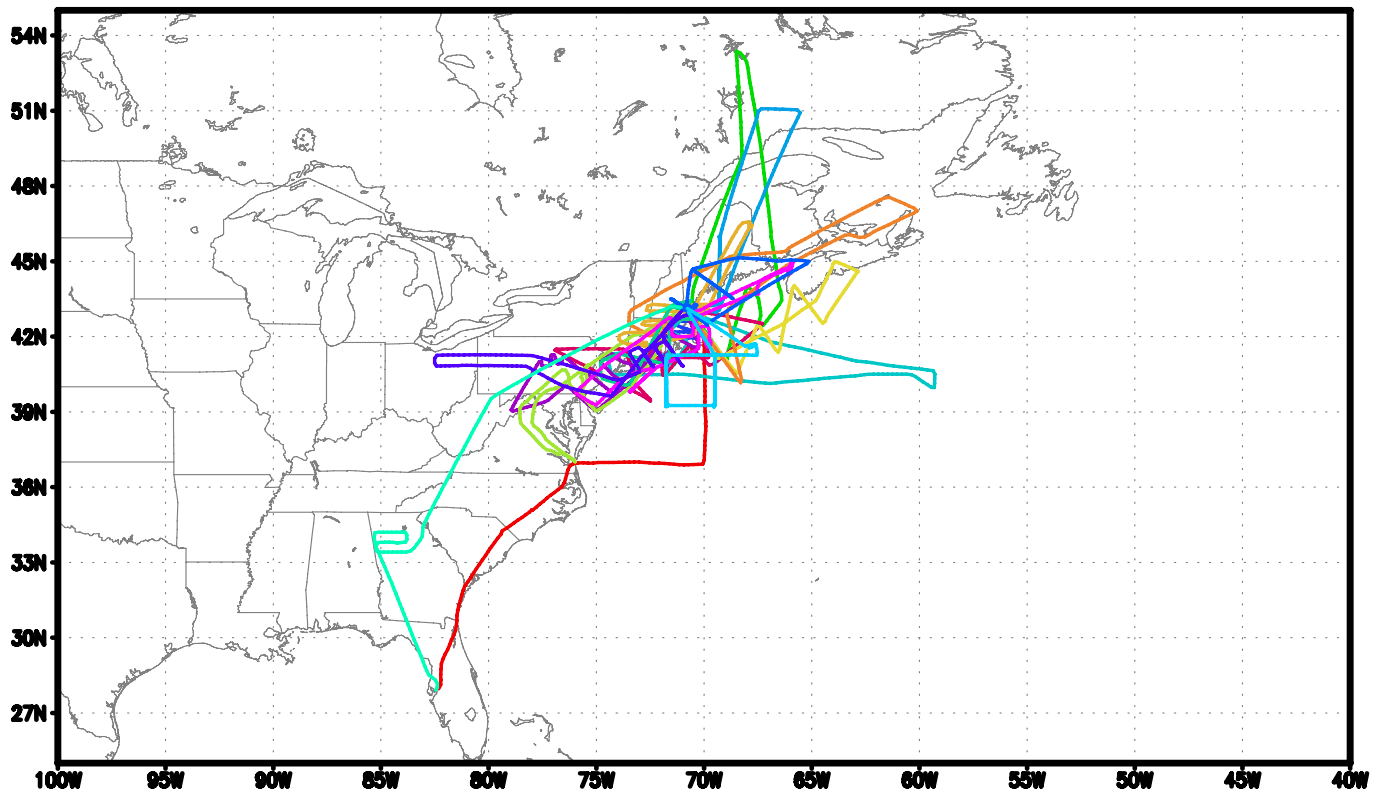


Figure 1. DC-8 and WP-3 flight paths during the ICARTT period. The colors show different flights.

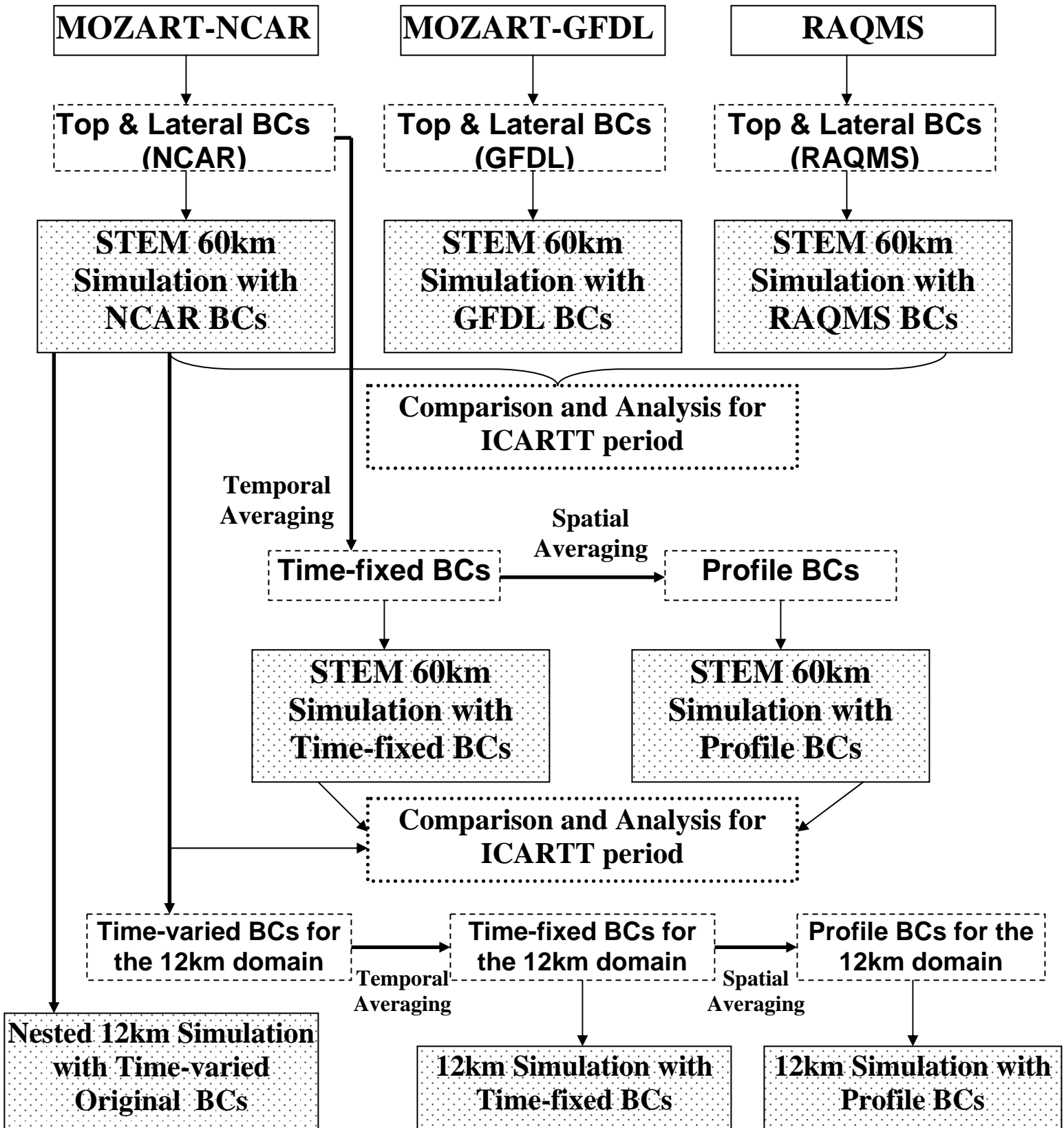
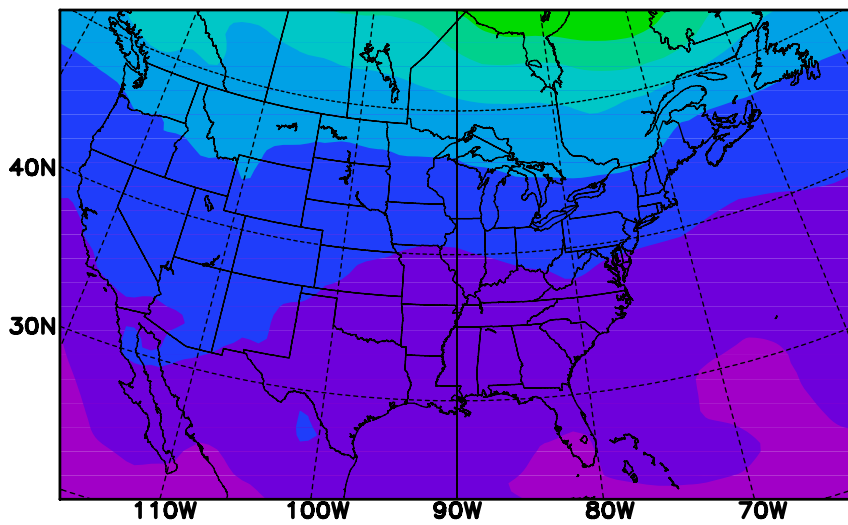
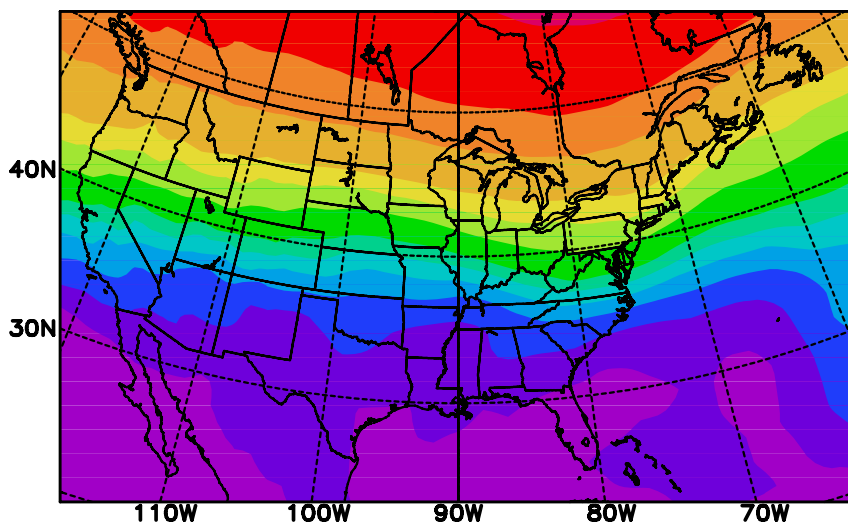


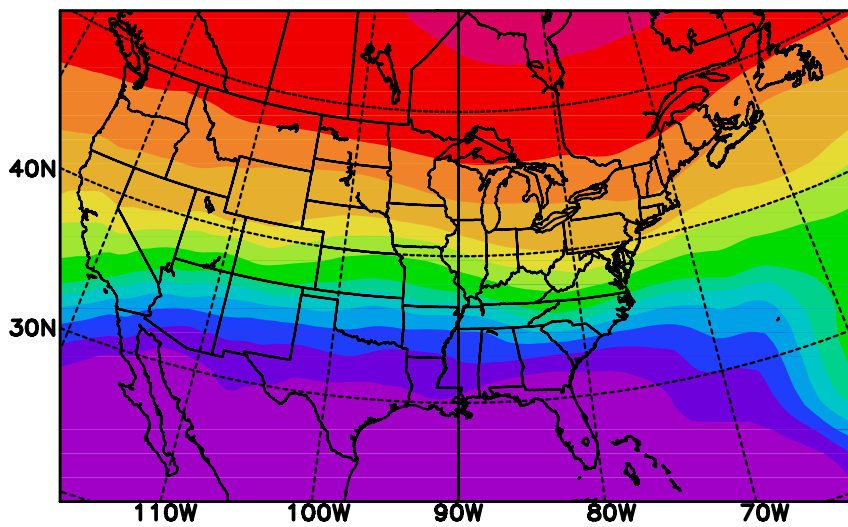
Figure 2. Comparison and Analysis Framework



MOZART-NCAR



MOZART-GFDL



RAQMS



Mean O₃ top boundary conditions (ppbv) during the ICARTT period

Figure 3. Period-mean O₃ top boundary conditions from 3 global models.

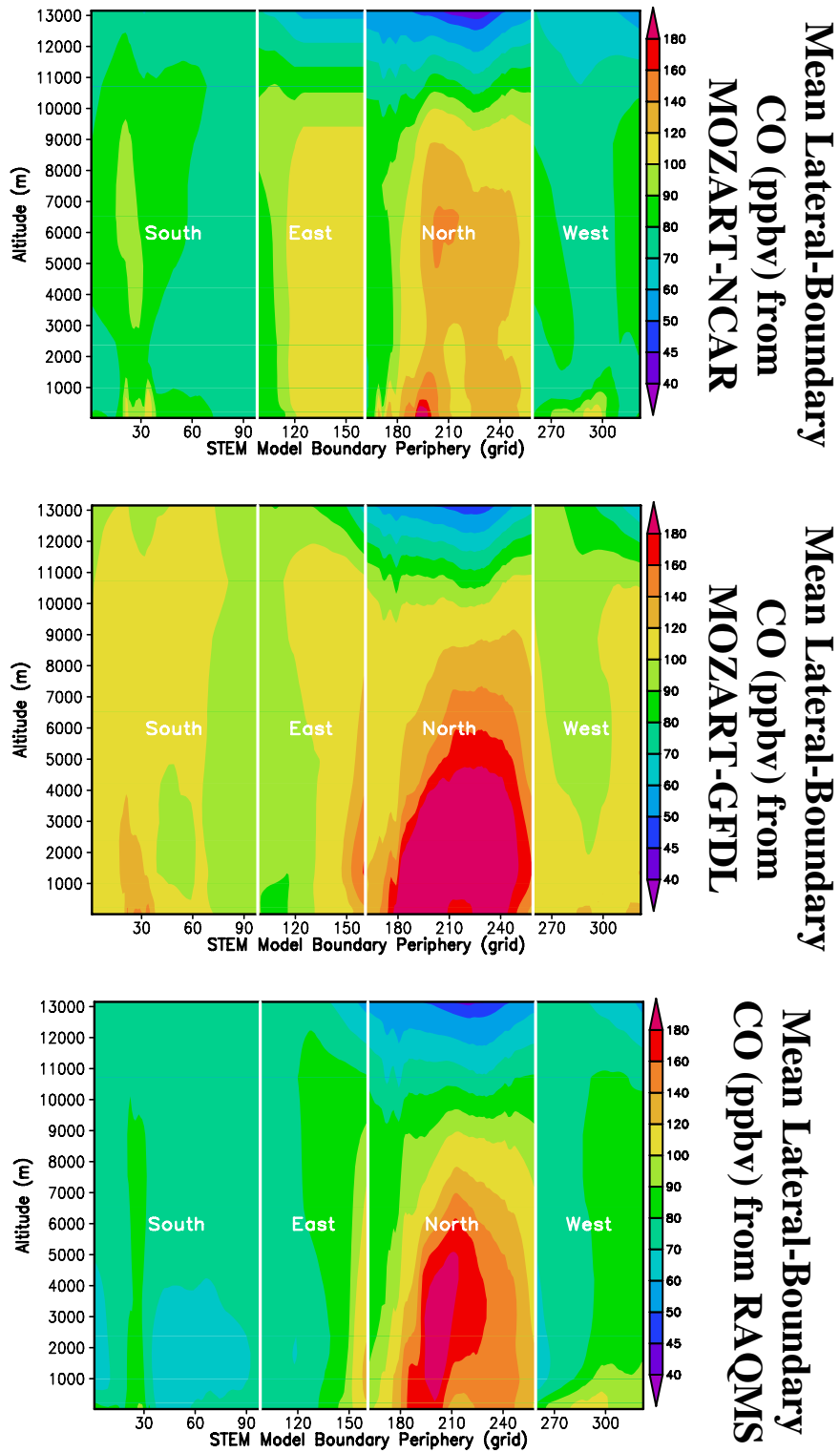


Figure 4. Period-mean CO lateral boundary conditions from 3 global models, along the STEM's boundary periphery in grid (60km) starting from the southwest corner of the STEM 60km domain shown in Figure 3.

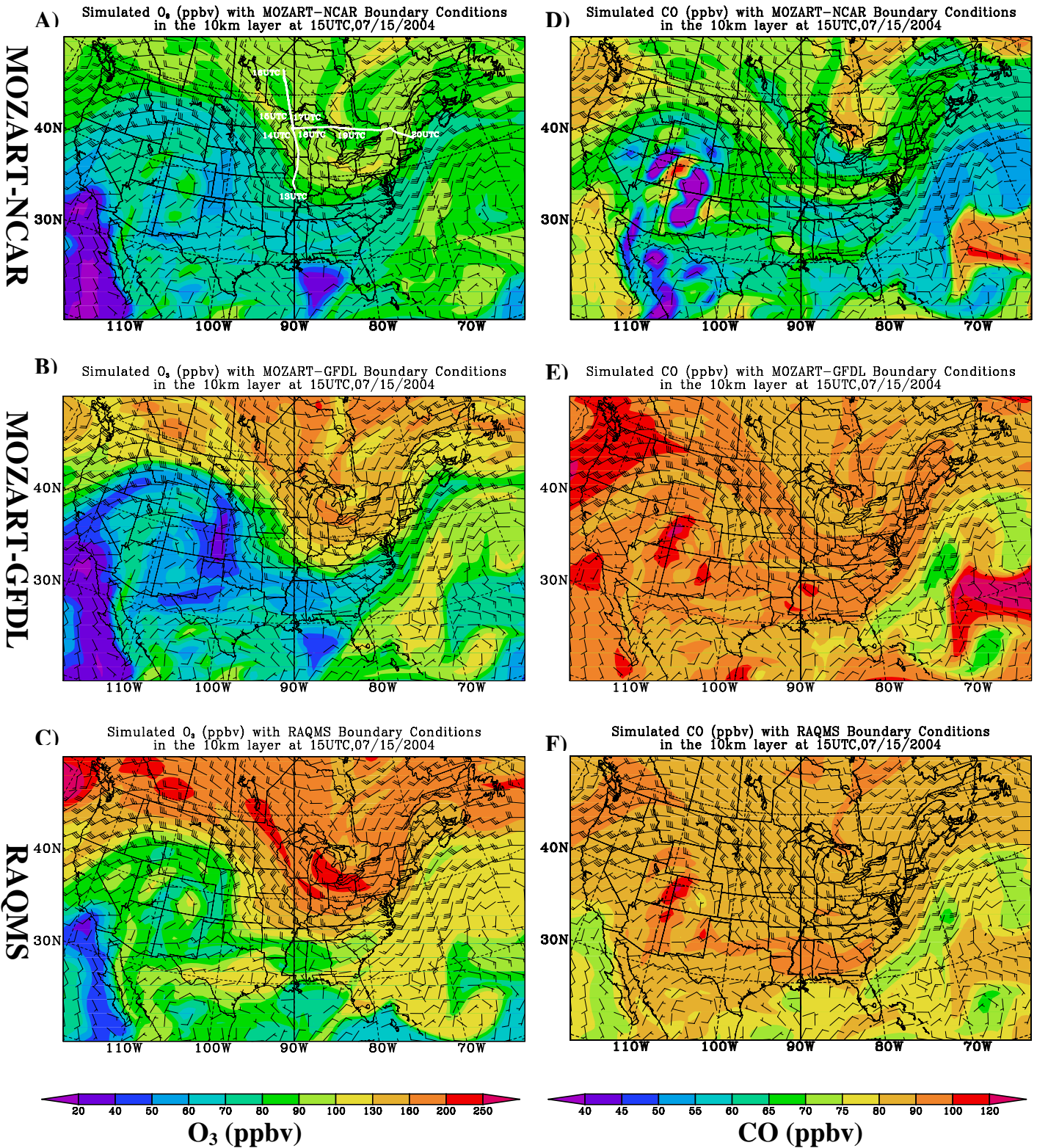


Figure 5. STEM 60km simulated O_3 and CO concentrations in the 10km layer with boundary conditions from the three global models for DC-8 flight 8 on July 15 (plot A shows the flight path).

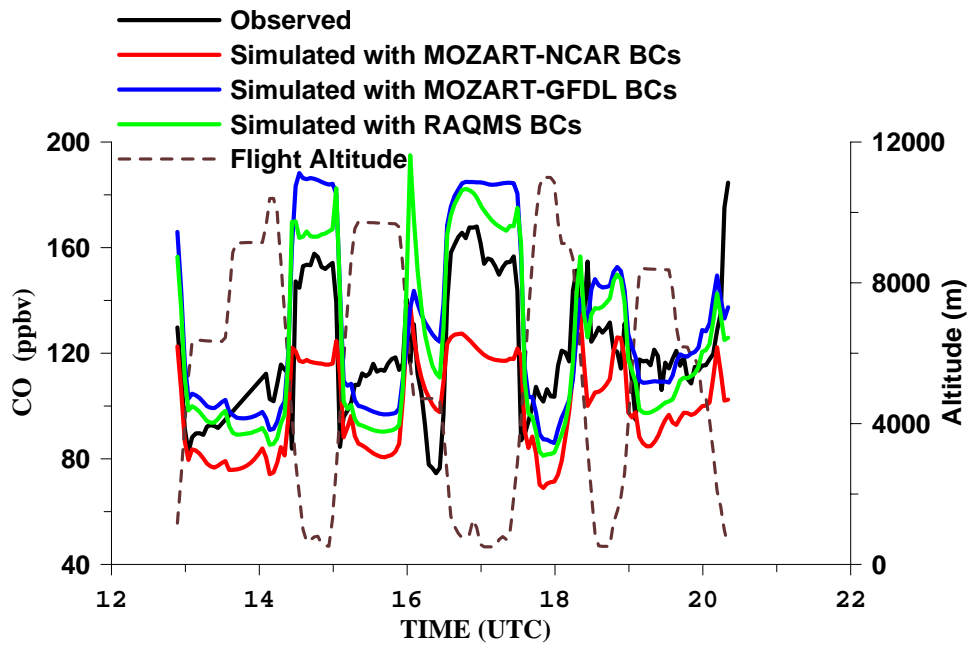
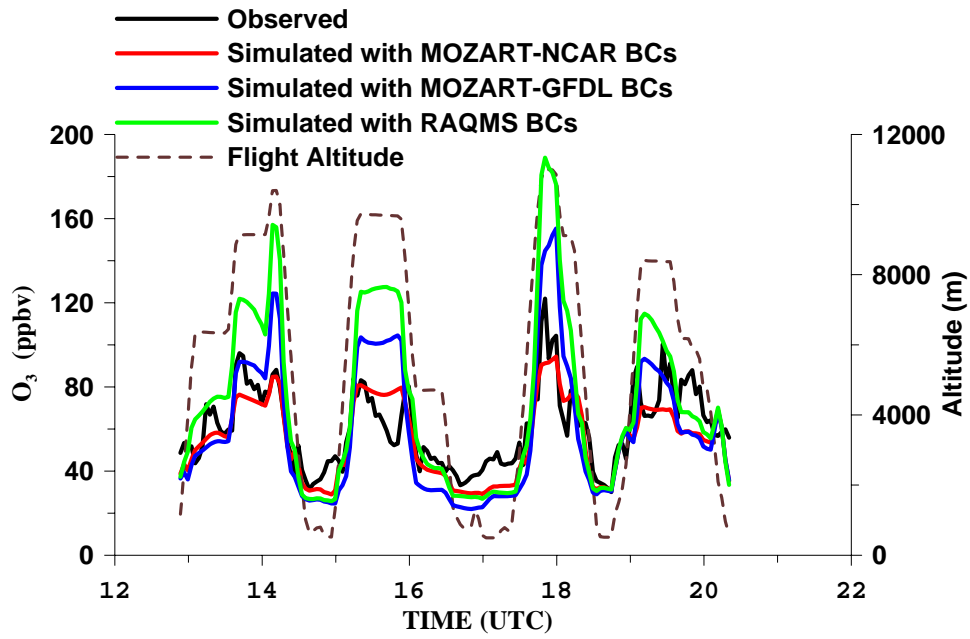


Figure 6. Observed and Simulated O₃ and CO concentrations for the DC-8 flight 8 on 07/15/2004

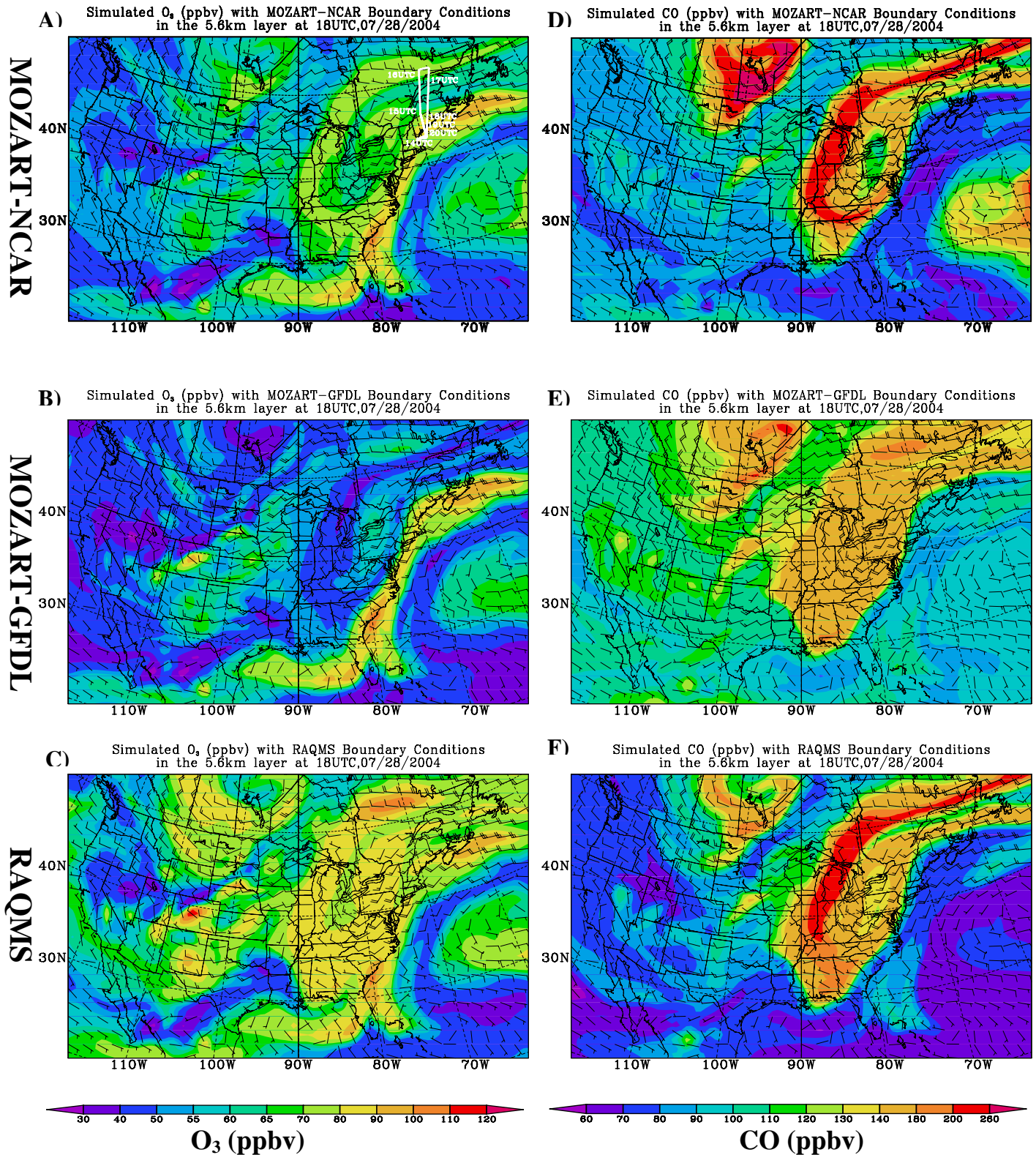


Figure 7. STEM 60km simulated O_3 and CO concentrations in the 5.6km layer with boundary conditions from the three global models for WP-3 flight 12 on July 28 (plot A shows the flight path).

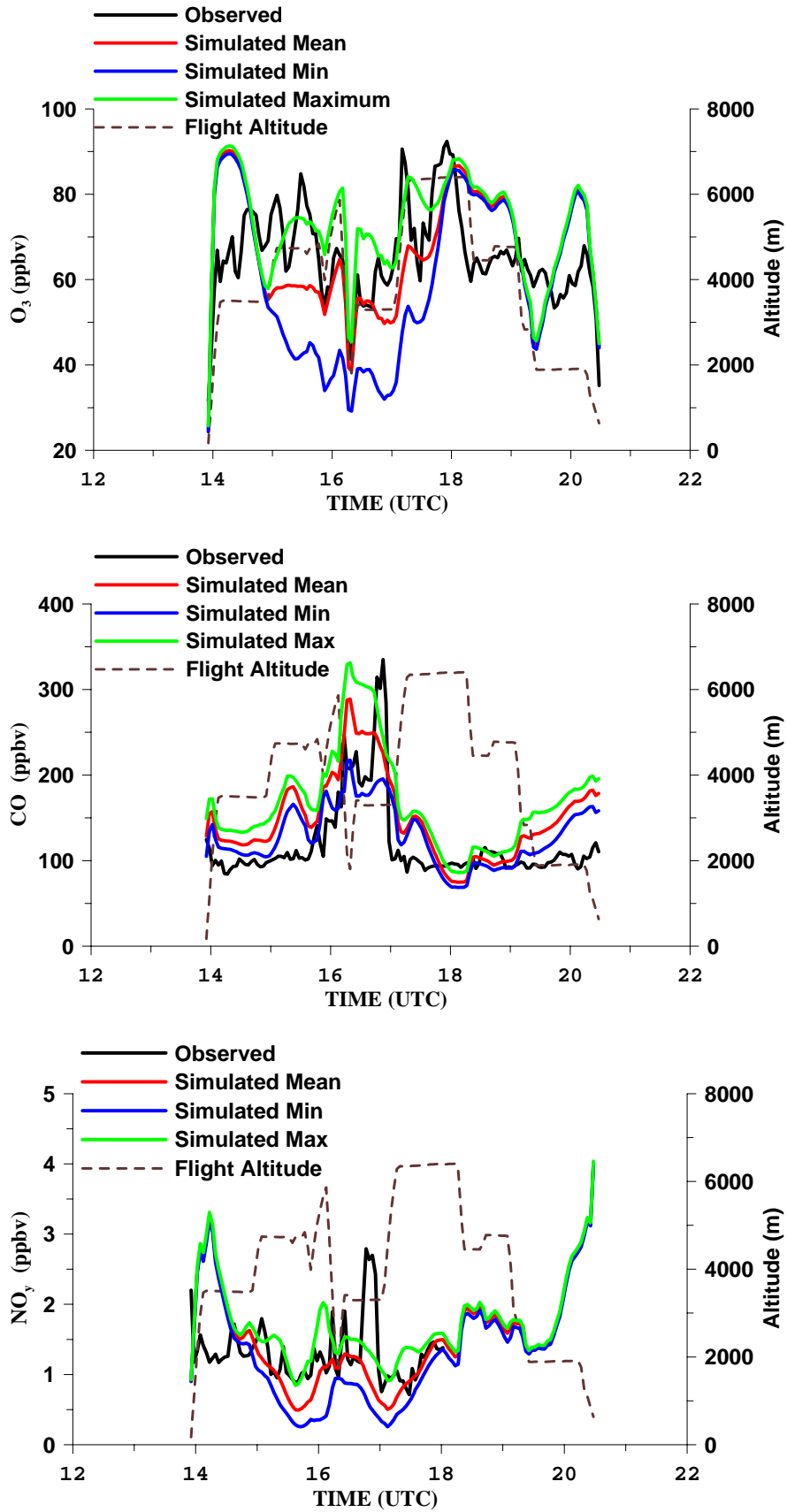


Figure 8. Observed and simulated mean/minimum/maximum O₃, CO, and NO_y concentrations for the WP-3 flight 12 on 07/28/2004

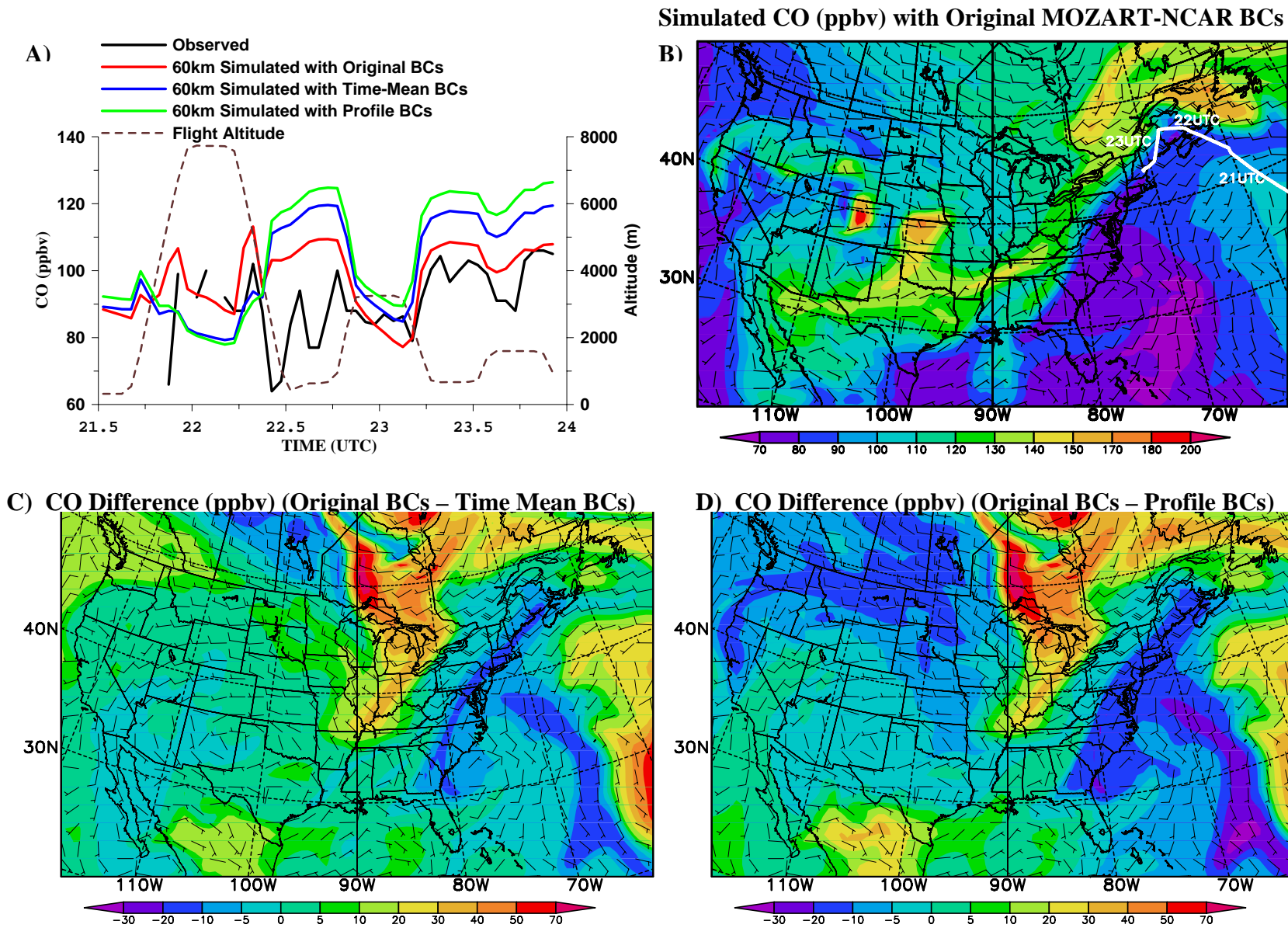


Figure 9. 60km simulated CO compared to the DC-8 flight observation on 07/31/2004. Plot B shows the simulated CO with original MOZART-NCAR BCs in the 3km layer, 0UTC, 08/01/2004. Plots C, D show the corresponding CO differences among the three simulations.

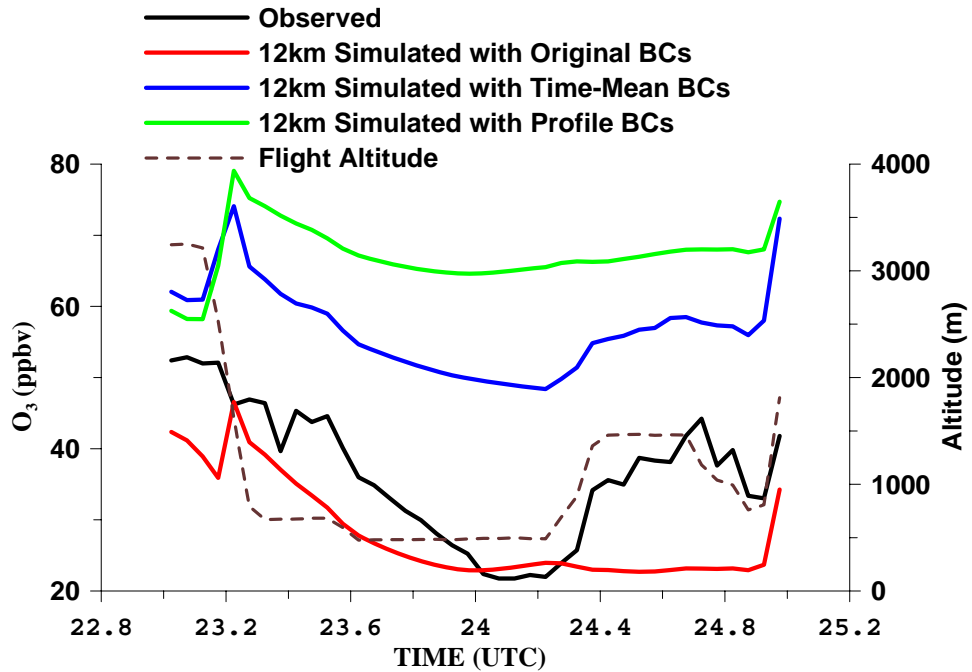
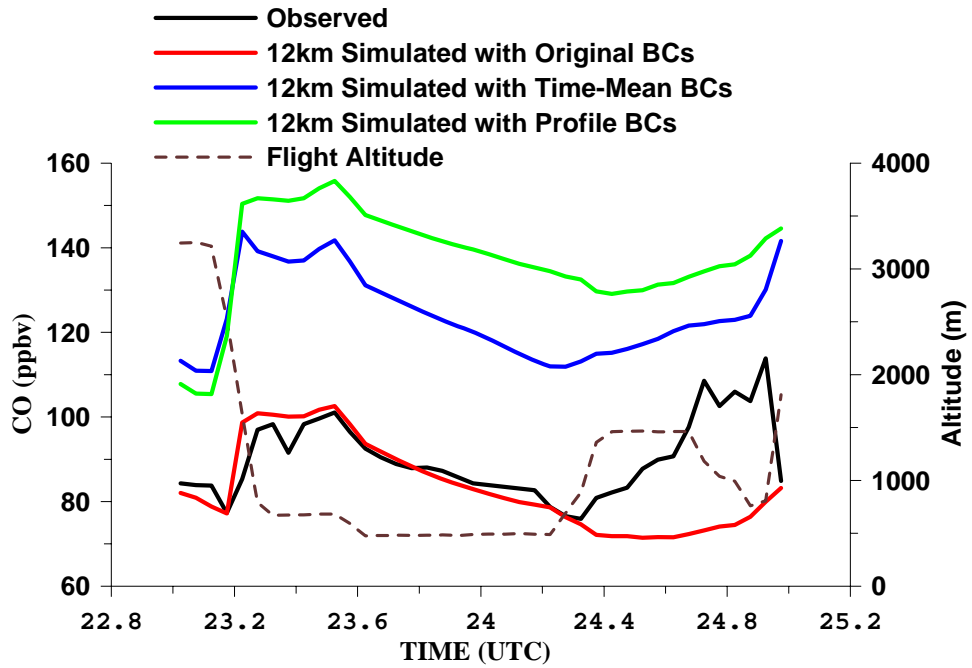


Figure 10. Observed and simulated CO and O₃ concentrations for the WP-3 flight 13 on 07/31- 08/01, 2004

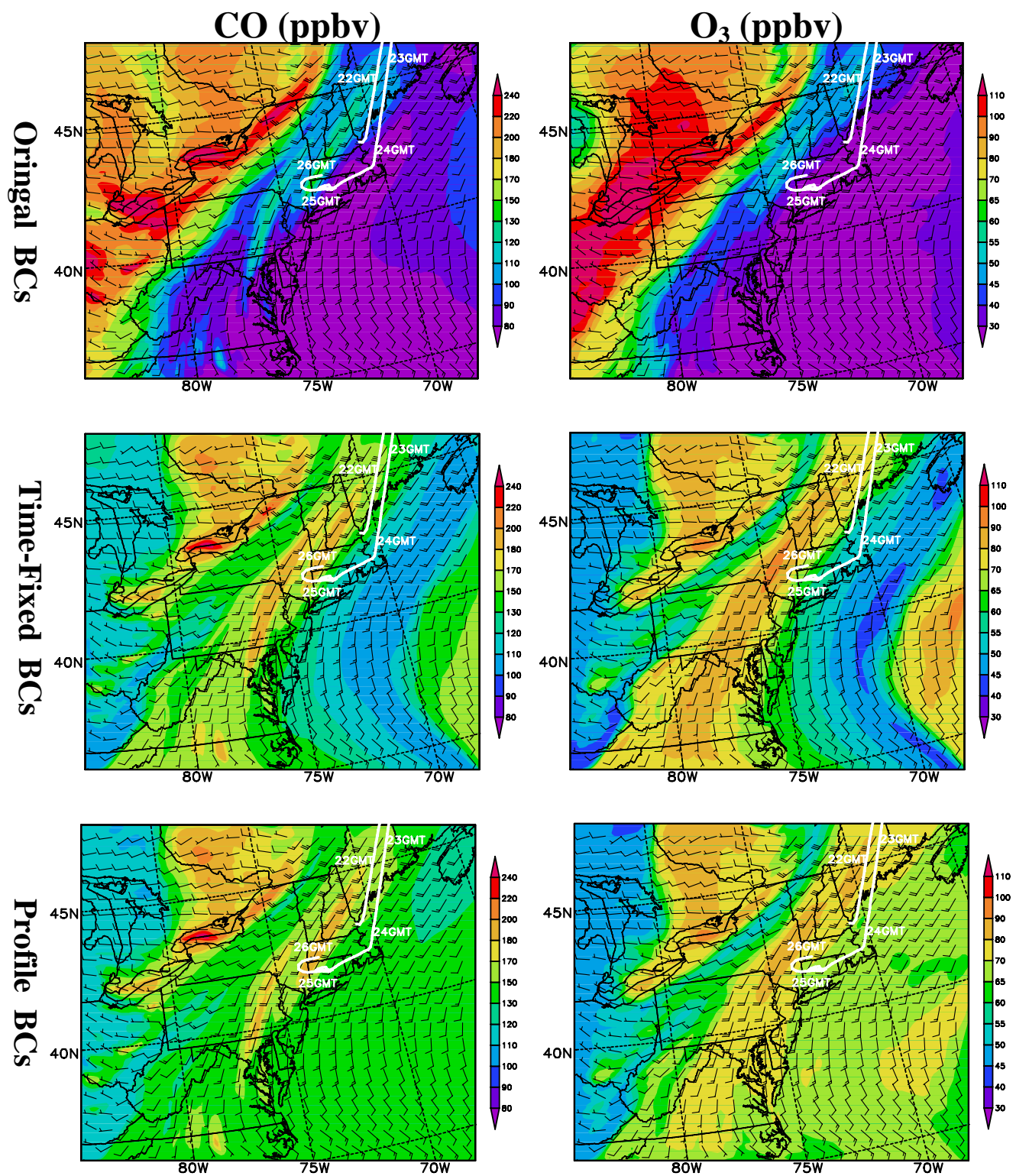


Figure 11. 12km simulated CO (left column) and O₃ (right column) concentrations in the 1km layer, at 0 UTC, 08/01/2004, driven by 3 different boundary conditions. The WP-3 flight path is shown in each plot.

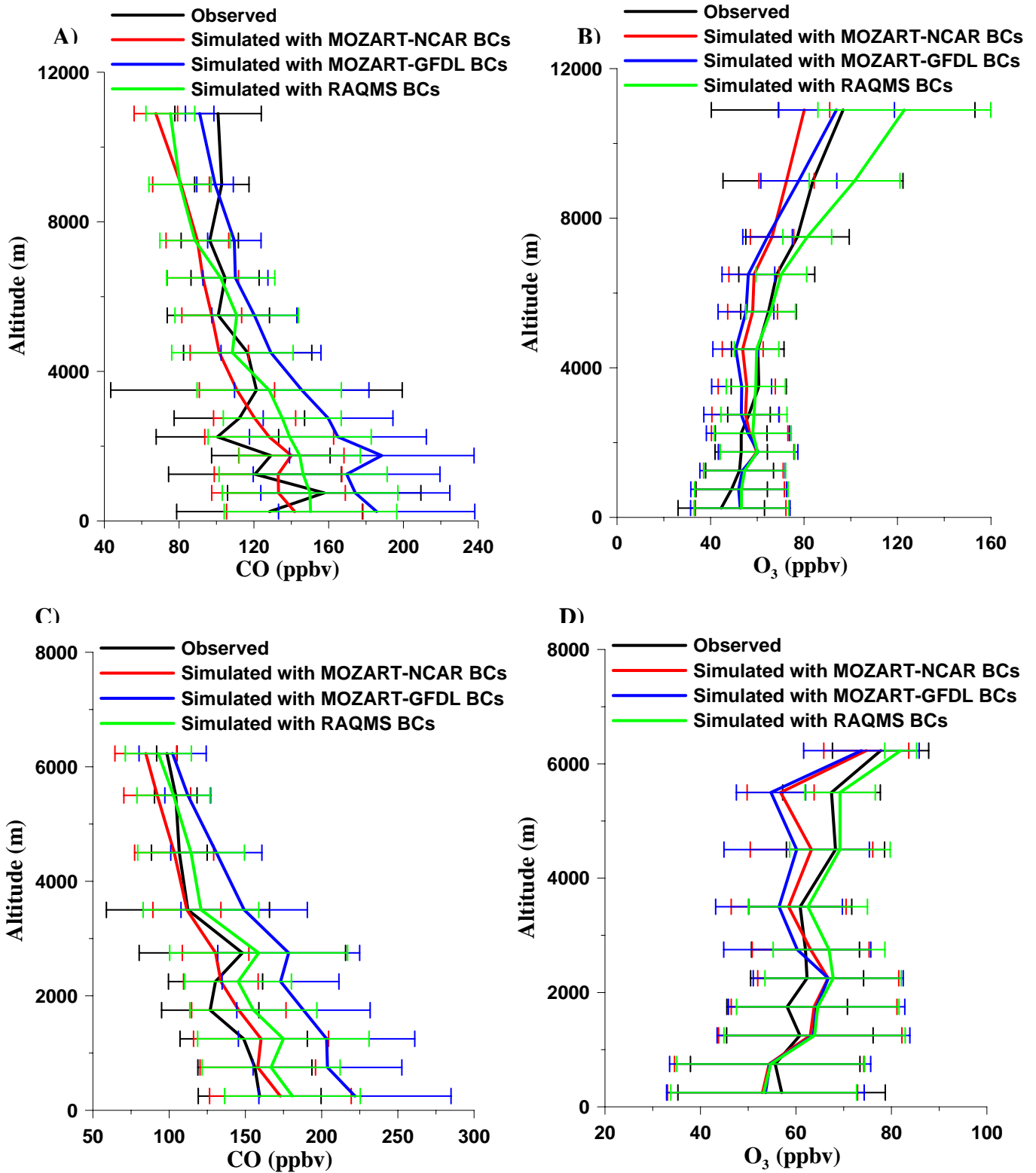


Figure 12. Observed and 60km-simulated CO and O₃ mean profiles and standard deviations for all DC-8 flights (A, B) and WP-3 flights (C, D)

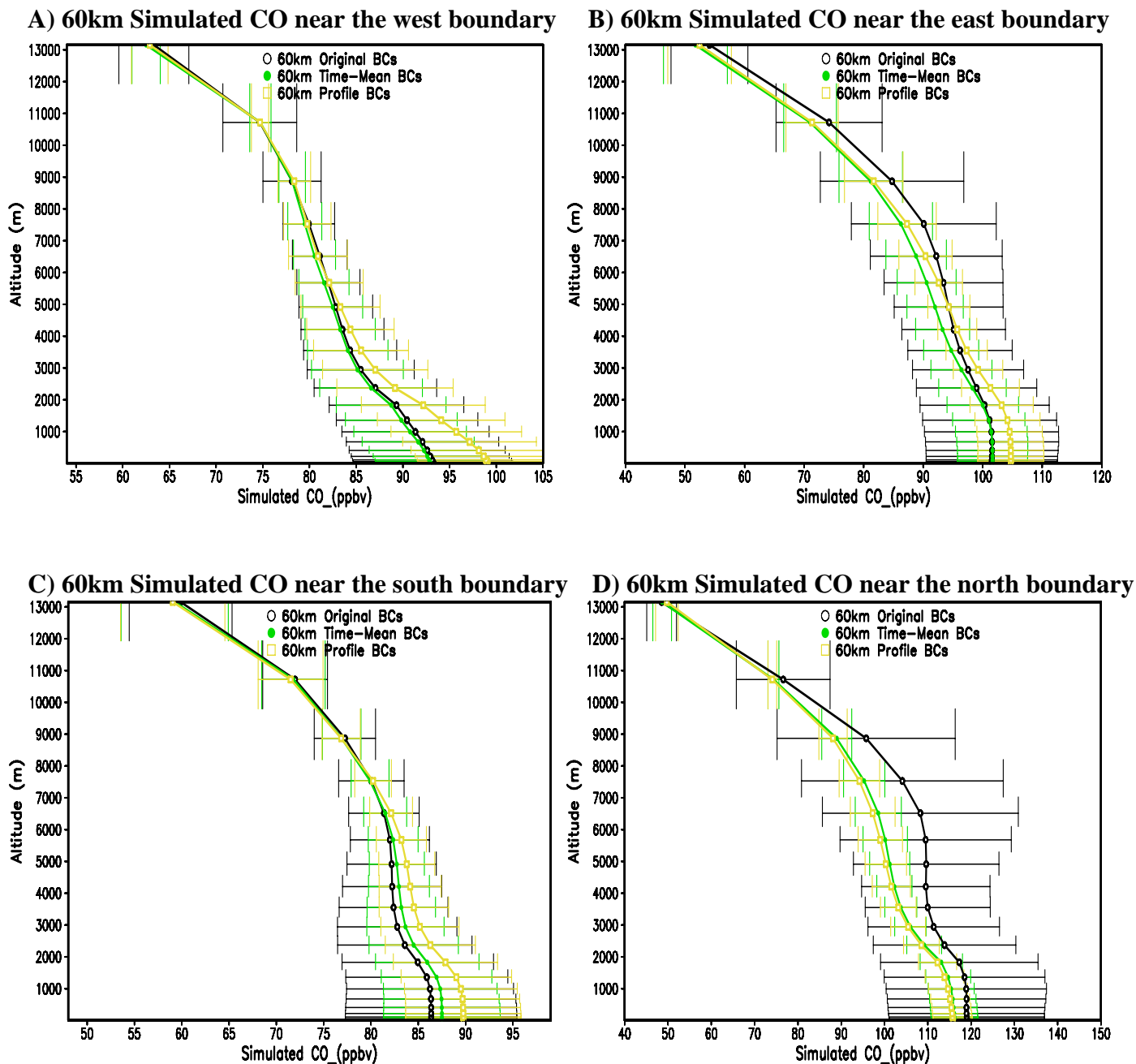


Figure 13. Simulated CO mean concentrations and standard deviation with original MOZART-NCAR, time-mean and profile boundary conditions over the grid lines that are 5 grid cells from west (A), east (B), south (C) and north (D) boundaries, respectively in the 60km domain.

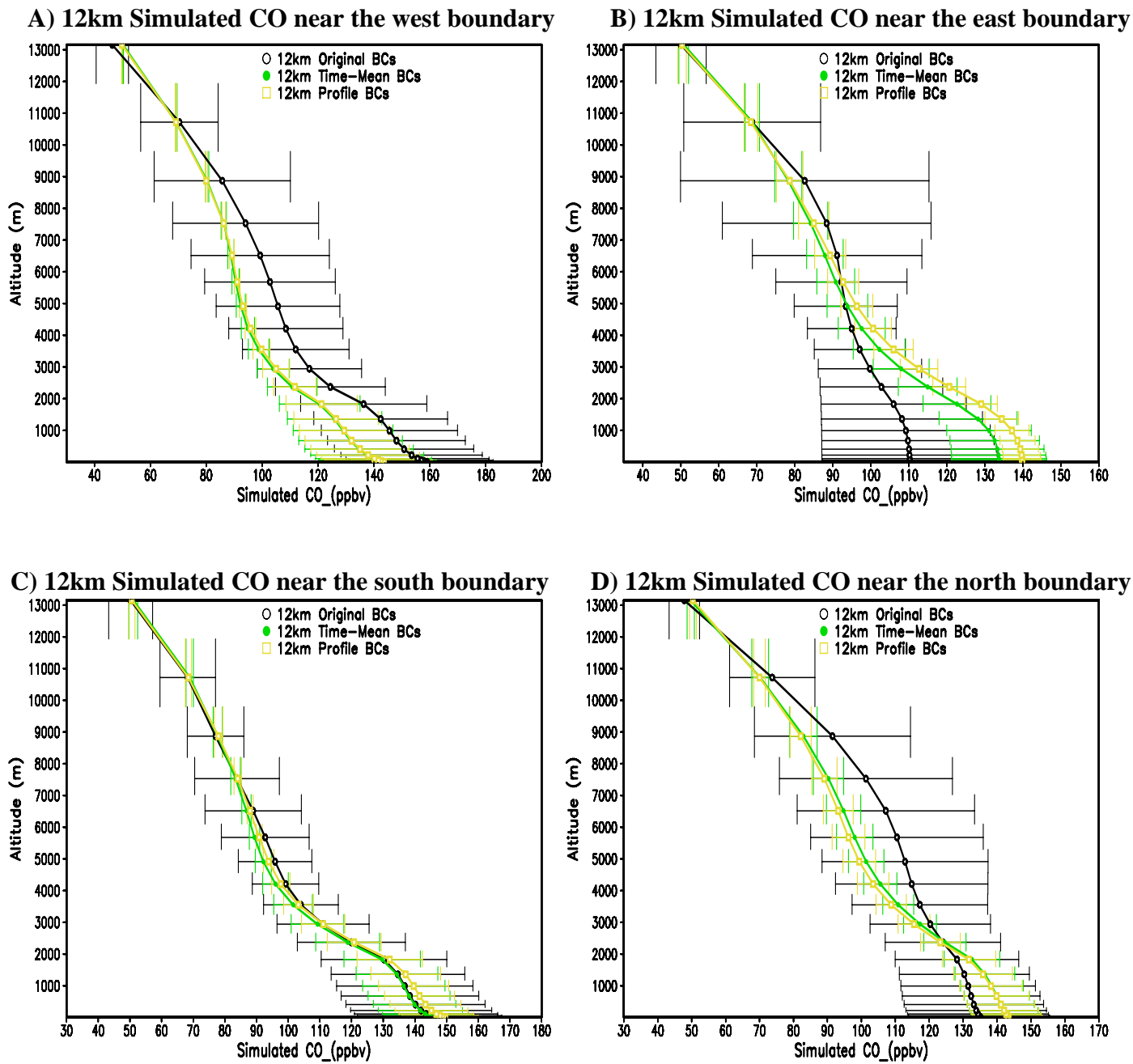


Figure 14. Simulated CO mean concentrations and standard deviation with original time-varied, time-mean and profile boundary conditions over the grid lines that are 5 grid cells from west (A), east (B), south (C) and north (D) boundaries, respectively in the 12km domain.

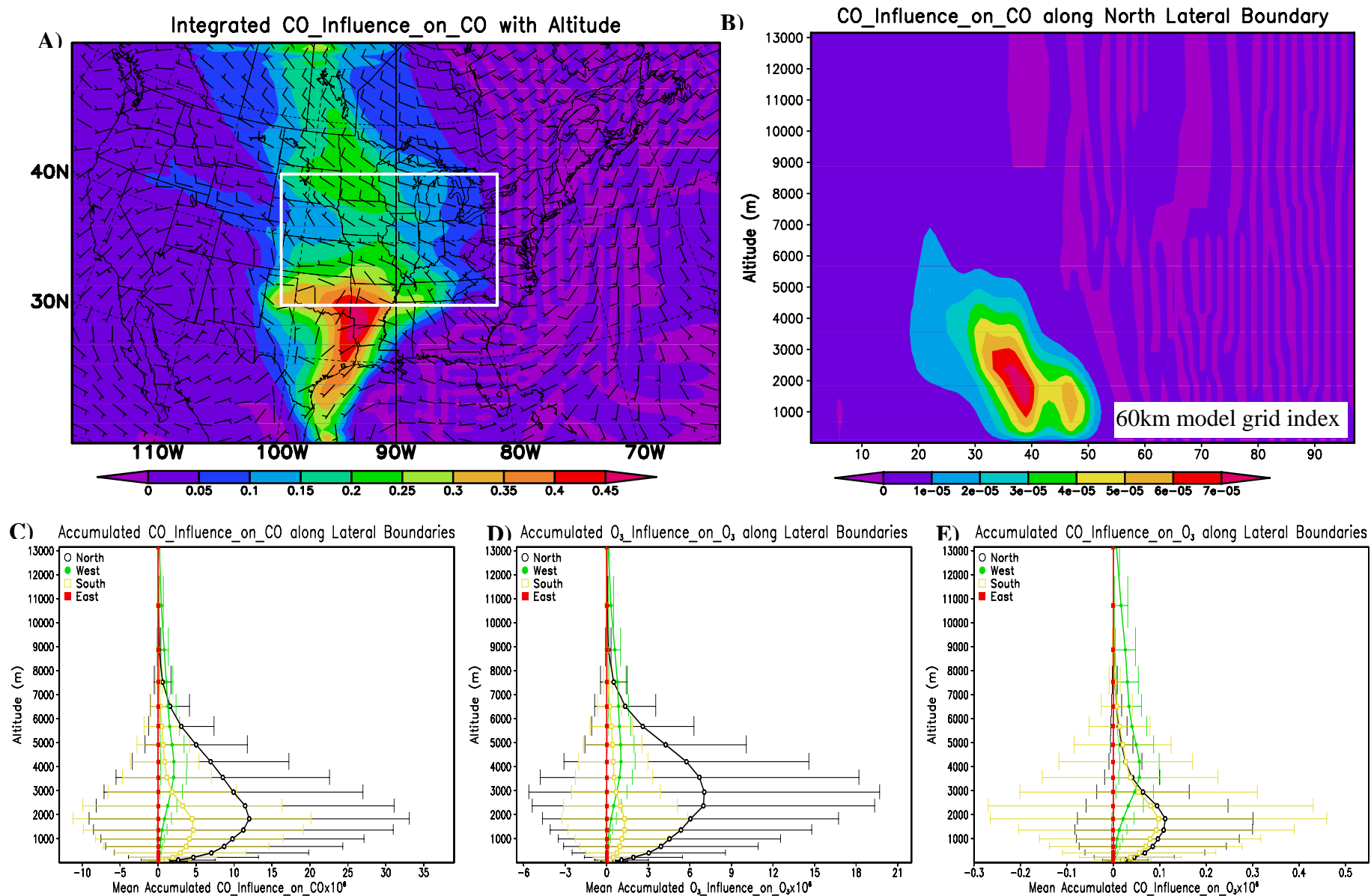


Figure 15. The influence function distributions: A) integrated with altitude and time-mean wind in 3km B) north boundary and C), D), E) mean and standard deviations along the 4 lateral boundaries. The influence functions are integrated from July 19 to 24 for the target grid box with vertical elevation 1-4km shown in panel A.